Economic Geology, v. 118, no. 5, pp. 1201–1217

SCIENTIFIC COMMUNICATIONS

APATITE VOLATILE CONTENTS OF PORPHYRY Cu DEPOSITS CONTROLLED BY DEPTH-RELATED FLUID EXSOLUTION PROCESSES

Ming-Liang Huang,[1] Jing-Jing Zhu,[1] Massimo Chiaradia,[2] Rui-Zhong Hu,[1, 3] Lei-Luo Xu,[1] and Xian-Wu Bi[1,†]

[1] *State Key Laboratory of Ore Deposit Geochemistry, Institute of Geochemistry, Chinese Academy of Sciences, Guiyang 550081, PR China*

[2] *Department of Earth Sciences, University of Geneva, rue des Maraîchers 13, Geneva 1205, Switzerland*

[3] *College of Earth and Planetary Sciences, University of Chinese Academy of Sciences, Beijing 100049, PR China*

Abstract

Porphyry Cu deposits are formed by Cu- and volatile (e.g., Cl, S)-rich fluids exsolved from underlying magma reservoirs. Intuitively, higher magmatic Cl and S contents likely correspond to higher magma fertility. However, the Cl contents of syn-ore magmatic apatite, one of the major Cl-bearing mineral phases in magmas, are highly variable among deposits (from <0.1 to >2 wt %). These variations may be controlled by different timing of apatite crystallization relative to fluid saturation among deposits, but the causes of these different relative timings remain obscure. Here we compile existing chemical data of magmatic apatite and amphibole phenocrysts from 25 porphyry Cu deposits worldwide and use these data to calculate magmatic physical-chemical conditions, such as water contents and magma reservoir depths. We find that the porphyry Cu deposits associated with deeper magma reservoirs are characterized by systematically higher magmatic H_2O contents and apatite Cl, but lower apatite F contents and F/Cl ratios compared to shallower deposits. These correlations are best explained by early fluid exsolution and Cl loss that predate apatite crystallization in shallower porphyry Cu systems, which leads to elevated apatite F/Cl ratios. This is supported by the common occurrence of primary fluid inclusions in apatite from shallower systems. Postsubduction porphyry Cu deposits are normally associated with lower apatite Cl contents and shallower magma reservoirs, which is attributed to their formation under relatively extensional tectonic regimes. Our results demonstrate that the magma reservoir depth exerts an important control on the timing of fluid exsolution and accompanying Cl loss. In contrast, relatively high and constant apatite S content among deposits is minimally affected by fluid exsolution, possibly due to buffering of early-saturated sulfate in oxidized and S-rich magmas, and therefore might be used as a better potential fertility indicator than Cl.

Introduction

Magmatic volatiles (e.g., Cl, S) play a crucial role in the formation of porphyry Cu-Mo-Au deposits that occur in magmatic arcs above oceanic subduction zones (syn-subduction setting; Cooke et al., 2005; Sillitoe, 2010; Richards, 2011) and in continent-collision or intracontinental settings (postsubduction setting; Hou et al., 2004; Richards, 2009; Holwell et al., 2019; Yang and Cooke, 2019). They act as key ligands to form metal complexes, which significantly enhance metal transfer from the magma to exsolving hydrothermal fluids, as well as metal carriers during hydrothermal evolution and sulfide precipitation (Shinohara, 1994; Zajacz et al., 2011). In view of this, high Cl and S contents are widely considered to be important in forming an economic porphyry Cu system (e.g., Cline and Bodnar, 1991; Imai, 2002; Zhu et al., 2018).

Magmatic volatile contents can be obtained through analysis of quenched glasses, including melt inclusions (e.g., Borisova et al., 2005; Zhang and Audétat, 2017; Stock et al., 2018), or be estimated from compositions of volatile-bearing minerals (e.g., apatite, amphibole, and biotite) by using published mineral/melt exchange or partition coefficients (e.g., Chelle-Michou and Chiaradia, 2017; Stock et al., 2018; Zhu et al., 2018; Cao et al., 2021; Li et al., 2021; Humphreys et al., 2021). Among the minerals of the latter method, apatite is most frequently used due to its capacity for accommodating abundant volatiles (e.g., S, Cl, F) in its crystal structure, as well as its resistance to postcrystallization physical and chemical weathering (Pan and Fleet, 2002; Mao et al., 2016).

Although many studies have measured higher apatite Cl and S contents of porphyry Cu-related intrusions than those of barren ones (Imai, 2002; Ishihara and Imai, 2014; Zhong et al., 2018; Zhu et al., 2018; Cao et al., 2021), an outstanding issue is that apatite Cl contents of synmineralization intrusions among porphyry Cu systems vary dramatically from <0.1 wt % (e.g., Yerington, Nevada; Streck and Dilles, 1998) to >2 wt % (e.g., Santo Tomas II and Clifton, Philippines; Imai, 2002), with low apatite Cl values mostly found in postsubduction porphyry Cu deposits in the Tibetan Plateau (<0.5 wt %; e.g., Qulong and Yulong, Tibet, China; Qin et al., 2014; Huang et al., 2019). The apatite F/Cl ratios among porphyry Cu deposits vary more dramatically from <1 (e.g., Santo Tomas II and Clifton, Philippines; Imai, 2002; Red Chris, Canada; Zhu et al., 2018) to >100 (e.g., Machangqing and Beiya, SW China; Wang et al., 2013, 2017; Yulong, east Tibet, China; Huang et al., 2019, 2022). Yet the reason for this remarkable variability remains unknown.

One possible explanation for the variability in apatite Cl contents and F/Cl ratios may be the influence of magma degassing and/or fluid exsolution processes (Cline and Bodnar, 1991; Stock et al., 2018), because Cl is preferentially partitioned

†Corresponding author: e-mail, bixianwu@vip.gyig.ac.cn

ISSN 0361-0128; doi:10.5382/econgeo.5000; 17 p.
Digital appendices are available in the online Supplements section.

Submitted: September 24, 2021/Accepted: October 19, 2022

into the exsolving aqueous fluids, whereas F is preferentially retained in the melt (Borodulin et al., 2009; Webster et al., 2009). To better understand the interplay between apatite volatile contents and these magmatic-hydrothermal processes, we have compiled over 1,000 published compositions of magmatic apatite as well as amphibole phenocrysts from 25 porphyry Cu deposits worldwide. The amphibole phenocryst data are used to estimate the depths of the magma reservoirs and the contents of H_2O in the parental magmas. With these data, we show that apatite Cl and F contents as well as F/Cl ratios in synmineralization intrusions are strongly controlled by the relative timing of fluid exsolution and apatite crystallization, which is likely further controlled by underlying magma reservoir depth. We also show that the apatite volatile composition and magma reservoir depth exhibit significant differences between synsubduction and postsubduction porphyry Cu systems. These differences are interpreted to reflect contrasting tectonic regimes during formation of synsubduction and postsubduction porphyry Cu systems.

Syn- and Postsubduction Porphyry Cu Deposits

Porphyry Cu-Mo-Au deposits are mostly found in continental and island arcs above oceanic subduction zones (synsubduction), particularly in the Pacific Rim (Richards, 2003; Cooke et al., 2005). They are genetically associated with relatively oxidized and hydrous calc-alkaline magmas that originated from sub-arc asthenospheric mantle that was metasomatized by fluids released by the subducting oceanic slab (Richards, 2003, 2011). The orebodies are developed around porphyritic intrusions (emplaced at ca. 2- to 5-km depth) and can also be hosted in wall rocks where reactive carbonate rocks are present (Sillitoe, 2010). The ore-forming fluids are thought to be exsolved from intermediate to felsic calc-alkaline magma reservoirs (ca. 5- to 15-km depth in the upper crust) upon extensive hydraulic fracturing of the magmatic carapace and surrounding country rocks due to buildup of pressure caused by accumulation of magmatic fluids in the cupola (Shinohara and Hedenquist, 1997; Cloos, 2001; Richards, 2003).

An increasing number of porphyry Cu-Mo-Au deposits are discovered in postsubduction settings in the Tethyan metallogenic domain (Hou et al., 2004, 2013, 2015; Richards, 2009; Shafiei et al., 2009; Xu et al., 2012, 2016; Yang et al., 2015, 2016; Zhou et al., 2015; Yang and Cooke, 2019). They are distinguished from their synsubduction counterparts by the lack of contemporaneous oceanic subduction but are consistent with collisional or intracontinental tectonic settings after the oceanic subduction was ceased (postsubduction). Mineralizing porphyry intrusions in postsubduction settings appear to be more alkali-rich, with high-K calc-alkaline to alkaline compositions (Richards, 2009; Chiaradia, 2020a), and are thought to originate from partial melting of previously subduction-modified arc lithosphere (Hou et al., 2004, 2013, 2015; Bi et al., 2005; Richards, 2009; Lu et al., 2013; Holwell et al., 2019; Yang and Cooke, 2019). Despite the source differences, they share broad similarities to subduction-related porphyry Cu deposits in terms of upper crustal ore-forming processes and geologic features, including being formed by magmatic fluids exsolved from underlying magma reservoirs (ca. 5–15 km depth) and characterized by zoned hydrothermal alteration patterns (Yang and Cooke, 2019).

Data Compilation and Filtering

We have compiled electron microprobe analyses of apatite and amphibole phenocrysts from 25 porphyry Cu deposits worldwide (Fig. 1), based on the following criteria:

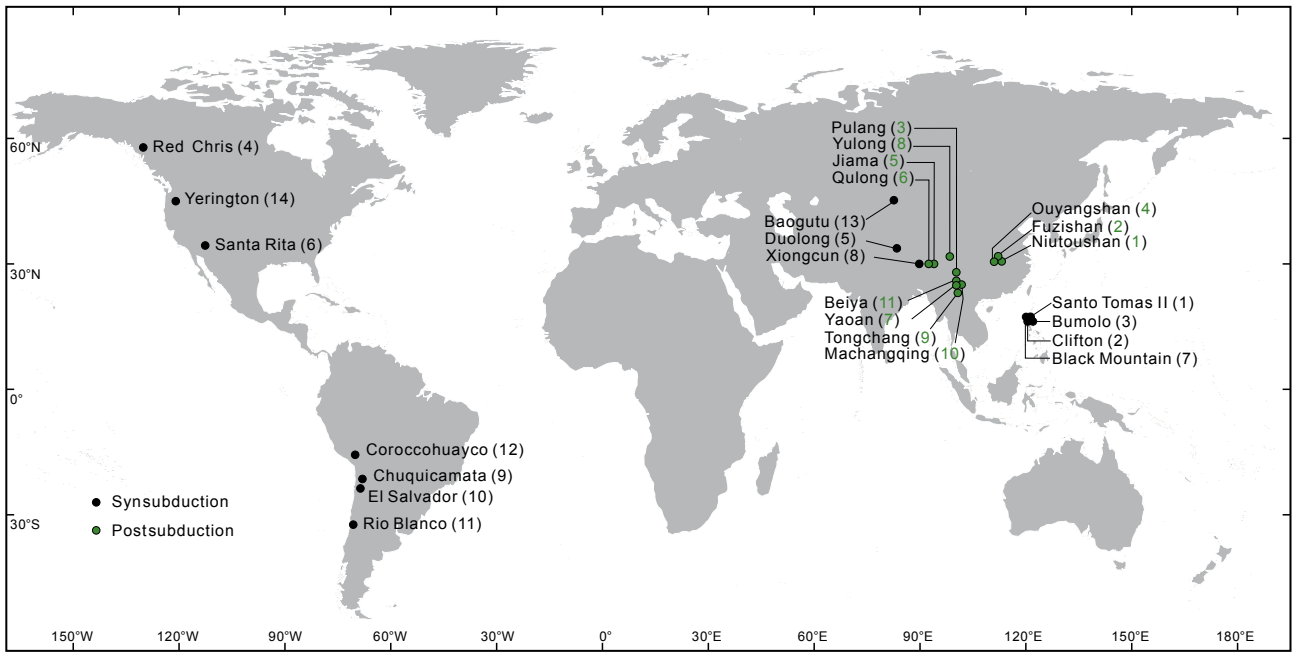

Fig. 1. Locations of porphyry Cu deposits compiled in this study. These deposits are grouped according to their tectonic settings (i.e., syn- and postsubduction settings) and numbered with decreasing apatite Cl contents (the numbers following deposit names are listed in Table 1).

1. The apatite should be of magmatic origin. Apatite crystals enclosed in fresh or least-altered magmatic minerals (e.g., amphibole, biotite, and zircon) are preferred because they are sheltered from hydrothermal alteration (Kendall-Langley et al., 2021). Most of our compiled apatites are of this type. Apatite data of a few deposits (i.e., Xiongcun in southern Tibet; Beiya, Machangqing, and Yaoan in western Yunnan) were obtained on grains with unclear petrographic context (Wang et al., 2013) or on grains separated from fresh igneous samples (Xie et al., 2018). Nonetheless, the analyzed apatite grains are shown to have euhedral shapes and oscillatory zonings in cathodoluminescence or backscattered electron images and are interpreted to be of magmatic origin (Wang et al., 2013; Xie et al., 2018).
2. The amphibole and apatite are from synmineralization intrusions, and those with inclusion relationships are preferred (e.g., apatite enclosed in amphibole phenocrysts; Coroccohuayco, Peru, Chelle-Michou et al., 2015; Chelle-Michou and Chiaradia, 2017; Qulong and Yulong, Tibet, China, Qin et al., 2014; Huang et al., 2022; Black Mountain, Philippines, Cao et al., 2018) because they have crystallized in equilibrium with each other. This is because when the amphibole phenocryst began to crystallize from the melt (700°–900°C according to the amphibole geothermometer of Ridolfi et al., 2010; App. Table A1), the enclosed apatite grains were likely in equilibrium with the same melt due to the high diffusivities of volatile species in apatite at those temperatures (Li et al., 2020).
3. Amphibole should occur as phenocrysts, which could preserve pristine information of the magma reservoir; data from xenomorphic (e.g., late-stage amphiboles crystallized from the groundmass) or xenocrystic amphiboles are excluded.
4. Apatites with F contents exceeding 3.76 wt % (maximum concentration in end-member fluorapatite) are excluded.

The compiled deposits are as follows: Santo Tomas II, Philippines; Clifton, Philippines; Bumolo, Philippines; Red Chris, Canada; Duolong, central Tibet; Santa Rita, New Mexico; Black Mountain, Philippines; Xiongcun, south Tibet; Chuquicamata, Chile; El Salvador, Chile; Rio Blanco, Chile; Coroccohuayco, Peru; Baogutu, northwest China; Yerington, Nevada; Niutoushan, east China; Fuzishan, east China; Ouyangshan, east China; Qulong, south Tibet; Pulang, southwest China; Jiama, south Tibet; Yao'an, southwest China; Yulong, east Tibet; Machangqing, southwest China; Tongchang, southwest China; Beiya, southwest China. Apatite compositions of the Jiama deposit are from this study. The analytical procedures are given in the Appendix. All the data and calculated magmatic physical-chemical conditions, such as H_2O contents and magma reservoir depths, are provided in Appendix Tables A1 and A2 and summarized in Table 1. These deposits are grouped according to their tectonic settings (i.e., synsubduction and postsubduction settings) and numbered according to decreasing apatite Cl contents (Fig. 1; Table 1).

Magmatic Water Contents and Magma Reservoir Depths

We have used amphibole composition to estimate magmatic water contents and magma reservoir depth. The compiled amphiboles are all classified as calcic amphiboles with $^{B}(Ca+\Sigma M^{2+})/\Sigma B$ values ≥ 0.75 and $^{B}Ca \geq {}^{B}\Sigma M^{2+}$ (Hawthorne et al., 2012; App. Table A1). In addition, the parental ore-forming magmas of these amphiboles are hydrous and calc-alkaline to high-K calc-alkaline in composition (App. Table A3; e.g., Chuquicamata and El Salvador in subduction setting: Baldwin and Pearce, 1982; Zentilli et al., 2018; Qulong and Yulong in postsubduction setting: Yang and Cooke, 2019). These features meet the criteria for using amphibole-based empirical calibrations (e.g., Schmidt, 1992; Anderson and Smith, 1995; Ridolfi et al., 2010; Ridolfi and Renzulli, 2012; Putirka, 2016; Mutch et al., 2016) to estimate magmatic physical-chemical conditions. In this study, magmatic water contents and temperatures are estimated using the methods of Ridolfi et al. (2010), which have been shown to yield reasonable results in porphyry systems (e.g., Red Chris, Zhu et al., 2018; Black Mountain, Cao et al., 2018; Pulang, Li et al., 2019). However, the geobarometer of Ridolfi et al. (2010) has been criticized because it likely reflects variations in magma composition and temperature (Erdmann et al., 2014; Putirka, 2016). Therefore, we utilize other amphibole geobarometers to estimate amphibole crystallization pressures (Hammarstrom and Zen, 1986; Hollister et al., 1987; Johnson and Rutherford, 1989; Thomas and Ernst, 1990; Schmidt, 1992; Mutch et al., 2016); results are presented in Figure 2 and Appendix Table A1. The different geobarometers yield positively correlated results, but many of them return impossible negative pressures for low-Al amphiboles (Fig. 2A-B; App. Table A1). The only exception is the geobarometer of Mutch et al. (2016), which requires that amphibole is in equilibrium with a mineral assemblage including quartz, plagioclase, and K-feldspar, consistent with the mineral assemblage of the calc-alkaline to high-K calc-alkaline ore-forming porphyries. Therefore, among all geobarometers tested, we retained the pressures provided by the geobarometer of Mutch et al. (2016). Magma reservoir depths were calculated from amphibole crystallization pressures, assuming conditions of lithostatic pressure ($\rho_{crust} = 2.7 \times 10^3$ kg/m^3). Estimated pressure (depth) and H_2O content returned by individual amphibole analysis are presented in Appendix Table A1, and the populations of several analyses from each deposit were averaged and tabulated in Table 1.

Recent studies have proposed that melt H_2O contents can also be estimated from apatite compositions or bulk rock compositions. The apatite hygrometer proposed by Li and Costa (2020; with a relative uncertainty of 30–40%; https://apthermo.wovodat.org) requires knowledge of apatite chemistry (at least CaO, P_2O_5, Cl, and F) and melt Cl and F contents. We have used the method of Li and Hermann (2017) to calculate melt Cl and F contents (App. Table A2) because this method is recognized to be built on experimental data obtained under conditions similar to ore-forming magmas (i.e., 0.2 GPa, ~900°C). Application of the hygrometer of Li and Costa (2020) to eligible deposits (i.e., the deposits where apatite CaO, P_2O_5, F, and Cl contents are all reported and are thus applicable to the apatite hygrometer) gives results for four deposits, two of which are equivalent to those estimated from the amphibole hygrometer (App. Fig. A1; App. Table A4). Nonetheless, apatite CaO and P_2O_5 contents are missing

Table 1. A Summary of Locations and Estimated Physical-Chemical Conditions of Synmineralization Intrusions from Porphyry Cu Deposits Compiled in this Study

Deposit	Deposit number[1]	Deposit type	Location	Age (Ma)	Apatite Cl contents (wt %)	1S.D.	R.Error (%)
Synsubduction setting							
Santo Tomas II	1	Porphyry Cu-Au	Baguio district of Northern Luzon, Philippines	1.5	3.39	0.82	5
Clifton	2	Porphyry Cu-Au	Baguio district of Northern Luzon, Philippines	1.7	3.20	0.93	-
Bumolo	3	Porphyry Cu-Au	Baguio district of Northern Luzon, Philippines	1.8	2.54	0.86	-
Red Chris	4	Porphyry Cu-Au	Stikinia island-arc terrane, northwest British Columbia	206.1	1.39	0.33	1
Duolong	5	Porphyry-epithermal Cu-Au	Duolong district, central Tibet	~118	1.36	0.51	2
Santa Rita	6	Porphyry Cu-Mo	Southwestern New Mexico, USA	52–72	1.31	0.08	3
Black Mountain	7	Porphyry Cu-Au	Baguio district of Northern Luzon, Philippines	2.83–2.98	1.29	0.08	4
Xiongcun	8	Porphyry Cu-Au	Jurassic Gangdese porphyry Cu belt, South Tibet	161.5–172.6	1.21	0.28	3
Chuquicamata	9	Porphyry Cu-Mo	Chuquicamata-El Abra porphyry copper belt, northern Chile	33.4	0.91	0.27	-
El Salvador	10	Porphyry Cu-Mo	Indio Muerto district, northern Chile	~42	0.44	0.04	-
Rio Blanco	11	Porphyry Cu-Mo	Late Tertiary magmatic belt, Central Chile	5.4-6.3	0.43	0.13	-
Coroccohuayco	12	Porphyry-skarn Fe-Cu-Au	Southern tip of the Andahuaylas-Yauri batholith, southern Peru	35.6	0.37	0.16	1
Baogutu	13	Porphryy Cu	Western Junggar of the central Asian orogenic belt	~310	0.35	0.12	-
Yerington	14	Porphyry Cu-Au	Yerington batholith, western Nevada, USA	168.7–170.0	0.06	0.03	6
Postsubduction setting							
Niutoushan	1	Porphyry-skarn Cu	Middle-lower Yangtze River belt, east China	137.8	0.47	0.08	3
Fuzishan	2	Porphyry-skarn Cu-Au	Middle-lower Yangtze River belt, east China	138.6	0.33	0.05	2
Pulang	3	Porphyry Cu-Au	Zhongdian belt, SW China	~216.5	0.29	0.19	1
Ouyangshan	4	Porphyry-skarn Cu	Middle-lower Yangtze River belt, east China	138.4	0.27	0.04	3
Jiama	5	Porphyry-skarn Cu-Au	Miocene Gangdese porphyry Cu belt, South Tibet	~15.4	0.27	0.02	4
Qulong	6	Porphyry Cu-Mo	Miocene Gangdese porphyry Cu belt, South Tibet	~16.1	0.26	0.07	3
Yaoan	7	Porphyry Au	Ailaoshan-Red River belt, SW China	~31.7	0.12	0.04	3
Yulong	8	Porphyry Cu-Mo	Yulong porphyry Cu belt, east Tibet, China	~42.28	0.08	0.02	2
Tongchang	9	Porphyry Cu-Mo	Ailaoshan-Red River belt, SW China	34.0	0.07	0.03	4
Machangqing	10	Porphyry Cu-Mo	Ailaoshan-Red River belt, SW China	~35.8	0.02	0.01	6
Beiya	11	Porphyry-skarn Au -Cu	Ailaoshan-Red River belt, SW China	36.8	0.01	0.00	5

Deposit	Deposit number[1]	Apatite F contents (wt %)	1S.D.	R.Error (%)	Apatite S contents (wt %)	1S.D.	R.Error (%)	Apatite F/Cl ratios	1S.D.	R.Error (%)	X_F	1S.D.	R.Error (%)
Synsubduction setting													
Santo Tomas II	1	1.35	0.36	7	0.11	0.01	5	0.4	0.2	8	0.36	0.10	5
Clifton	2	1.26	0.30	-	0.12	0.06	-	0.4	-	-	0.33	-	-
Bumolo	3	1.77	0.44	-	0.08	0.06	-	0.7	-	-	0.47	-	-
Red Chris	4	2.32	0.24	1	0.12	0.07	1	1.8	0.8	1	0.62	0.06	1
Duolong	5	1.92	0.44	2	0.15	0.11	2	2.3	3.2	4	0.51	0.12	2
Santa Rita	6	2.22	0.17	3	0.09	0.04	3	1.7	0.2	4	0.59	0.05	3
Black Mountain	7	1.09	0.08	4	0.12	0.07	4	0.8	0.1	5	0.29	0.02	4
Xiongcun	8	2.41	0.29	3	0.02	0.01	3	2.1	0.7	4	0.64	0.08	3
Chuquicamata	9	2.72	0.31	-	0.08	-	-	3.0	-	-	0.72	-	-
El Salvador	10	2.91	0.24	-	0.07	-	-	6.6	-	-	0.77	-	-
Rio Blanco	11	3.14	0.40	-	0.02	-	-	7.3	-	-	0.83	-	-
Coroccohuayco	12	2.90	0.31	1	0.10	0.05	1	10	5.5	2	0.77	0.08	1
Baogutu	13	3.06	0.29	-	0.06	0.04	-	8.7	-	-	0.81	-	-
Yerington	14	3.59	0.10	6	-	-	-	73	41	9	0.95	0.03	6
Postsubduction setting													
Niutoushan	1	2.20	0.26	3	0.10	0.03	3	4.9	1.5	4	0.59	0.07	3
Fuzishan	2	2.48	0.38	2	0.12	0.08	3	7.7	2.0	3	0.66	0.10	2
Pulang	3	2.84	0.28	1	0.09	0.05	1	19	21	2	0.75	0.07	1
Ouyangshan	4	2.27	0.29	3	0.17	0.05	3	8.7	2.0	4	0.60	0.08	3
Jiama	5	3.09	0.17	4	0.15	0.11	4	12	1.2	5	0.82	0.04	4
Qulong	6	3.30	0.16	3	0.08	0.04	3	15	7.9	4	0.88	0.04	3
Yaoan	7	3.05	0.20	3	0.07	0.04	4	28	9	5	0.81	0.05	3
Yulong	8	2.45	0.14	2	0.14	0.09	2	33	13	3	0.65	0.04	2
Tongchang	9	3.21	0.17	4	0.05	0.03	4	50	17	4	0.85	0.04	4
Machangqing	10	3.60	0.03	6	0.02	0.01	6	160	35	6	0.95	0.01	6
Beiya	11	2.91	0.68	5	0.29	0.10	5	388	144	5	0.77	0.18	5

Table 1 (*Cont.*)

Deposit	Deposit number[1]	X_{Cl}	1S.D.	R.Error (%)	X_{OH}	1S.D.	R.Error (%)	Amphibole crystallizing temperature (°C)	1S.D.	R.Error (%)	Magmatic H_2O contents (wt %)	1S.D.	R.Error (%)
Synsubduction setting													
Santo Tomas II	1	0.50	0.12	5	0.14	0.03	22	833	-	-	6.3	-	-
Clifton	2	0.47	-	-	0.20	-	-	892	-	-	7.0	-	-
Bumolo	3	0.37	-	-	0.16	-	-	841	-	-	5.7	-	-
Red Chris	4	0.20	0.05	1	0.18	0.05	3	900	30	0	5.1	0.4	2
Duolong	5	0.20	0.08	2	0.29	0.08	3	839	38	0	5.4	0.6	1
Santa Rita	6	0.19	0.01	3	0.22	0.04	8	800	5	2	4.6	0.2	6
Black Mountain	7	0.19	0.01	4	0.52	0.03	2	856	5	1	6.2	0.0	3
Xiongcun	8	0.18	0.04	3	0.18	0.07	10	773	43	1	4.6	1.0	3
Chuquicamata	9	0.13	-	-	0.14	-	-	735	-	-	3.8	-	-
El Salvador	10	0.06	-	-	0.16	-	-	732	-	-	3.1	-	-
Rio Blanco	11	0.06	-	-	0.10	-	-	730	-	-	3.8	-	-
Coroccohuayco	12	0.05	0.02	1	0.18	0.06	5	781	31	0	4.2	0.4	1
Baogutu	13	0.05	-	-	0.14	-	-	800	15	0	4.3	0.4	2
Yerington	14	0.01	0.00	6	0.04	0.03	141	754	39	2	4.1	0.3	7
Postsubduction setting													
Niutoushan	1	0.07	0.01	3	0.35	0.07	4	782	27	1	4.3	0.2	2
Fuzishan	2	0.05	0.01	2	0.29	0.10	5	753	30	1	4.4	0.2	2
Pulang	3	0.04	0.03	1	0.20	0.06	4	789	6	1	4.3	0.7	4
Ouyangshan	4	0.04	0.01	3	0.36	0.08	4	792	13	1	4.1	0.2	2
Jiama	5	0.04	0.00	4	0.14	0.05	22	778	11	1	4.1	0.2	2
Qulong	6	0.04	0.01	3	0.09	0.04	27	773	11	1	3.7	0.5	2
Yaoan	7	0.02	0.01	3	0.17	0.05	15	845	12	1	3.1	0.1	6
Yulong	8	0.01	0.00	2	0.34	0.04	3	807	20	1	4.2	0.3	2
Tongchang	9	0.01	0.00	4	0.14	0.04	23	825	22	1	4.1	0.1	2
Machangqing	10	0.00	0.00	6	0.04	0.01	132	747	37	1	3.5	0.4	2
Beiya	11	0.00	0.00	5	0.23	0.18	17	709	31	1	3.3	0.5	4

Deposit	Deposit number[1]	Amphibole crystallizing pressure (kbar)	1S.D.	R.Error (%)	Magma reservoir depth (km)	1S.D.	R.Error (%)	Reference
Synsubduction setting								
Santo Tomas II	1	3.1	-	-	12.0	-	-	Imai (2001, 2002)
Clifton	2	4.4	-	-	16.7	-	-	Imai (2001, 2002)
Bumolo	3	3.1	-	-	11.8	-	-	Imai (2001, 2002)
Red Chris	4	4.7	0.8	2	17.7	3.2	2	Zhu et al. (2018)
Duolong	5	3.3	0.8	2	12.4	3.0	2	Li et al. (2018, 2020)
Santa Rita	6	2.3	0.1	11	8.7	0.4	11	Audétat et al. (2004)
Black Mountain	7	3.6	0.1	8	13.8	0.3	8	Hollings et al. (2013); Cao et al. (2018)
Xiongcun	8	1.9	0.9	6	7.3	3.4	6	Xie et al. (2018, 2020)
Chuquicamata	9	1.2	-	-	4.7	-	-	Ballard et al. (2001); Ishihara and Imai (2014)
El Salvador	10	1.1	-	-	4.4	-	-	Ishihara and Imai (2014); Lee et al. (2017)
Rio Blanco	11	1.2	-	-	4.6	-	-	Deckart et al. (2005); Ishihara and Imai (2014)
Coroccohuayco	12	2.0	0.6	1	7.8	2.1	1	Cyril-Chelle-Michou et al. (2015); Cyril-Chelle-Michou and Chiaradia (2017)
Baogutu	13	2.2	0.3	3	8.3	1.0	3	Shen and Pan (2013); Cao et al. (2015)
Yerington	14	1.4	0.2	11	5.4	0.9	11	Dilles (1987); Banik et al. (2017)
Postsubduction setting								
Niutoushan	1	1.9	0.4	4	7.2	1.5	4	Duan (2019)
Fuzishan	2	1.7	0.4	4	6.3	1.5	4	Duan (2019)
Pulang	3	2.1	0.2	7	7.9	0.9	7	Pan et al. (2016); Leng et al. (2018)
Ouyangshan	4	1.9	0.2	4	7.4	0.7	4	Duan (2019)
Jiama	5	1.9	0.1	4	7.4	0.6	4	Wang et al. (2014); this study
Qulong	6	1.7	0.2	3	6.6	0.6	3	Wang et al. (2014); Qin et al. (2014)
Yaoan	7	3.0	0.1	8	11.5	0.6	8	Bi et al. (2009); Wang et al. (2013)
Yulong	8	2.5	0.4	3	9.5	1.4	3	Huang et al. (2019a, 2019b, 2022)
Tongchang	9	3.1	0.5	4	11.9	1.8	4	Wang et al. (2013); Xu et al. (2012); Xu et al. (2023)
Machangqing	10	1.5	0.4	3	5.6	1.6	3	Wang et al. (2013); Xu et al. (2012); Shen et al. (2018)
Beiya	11	1.2	0.3	6	4.5	1.3	6	Wang et al. (2013); Wang et al.(2017)

Notes: S.D. = standard deviation; R.Error (relative errors in %) for apatite compositions and X_{Cl}, X_F, and X_{OH} values are propagated from the uncertainties of analytical results; R.Error (relative errors in %) for physical-chemical conditions of the magma are propagated from the uncertainties of amphibole calculation results in Appendix Table A1

[1]The deposits are grouped according to their tectonic settings (i.e., synsubduction and postsubduction settings), and numbered with decreasing apatite Cl contents

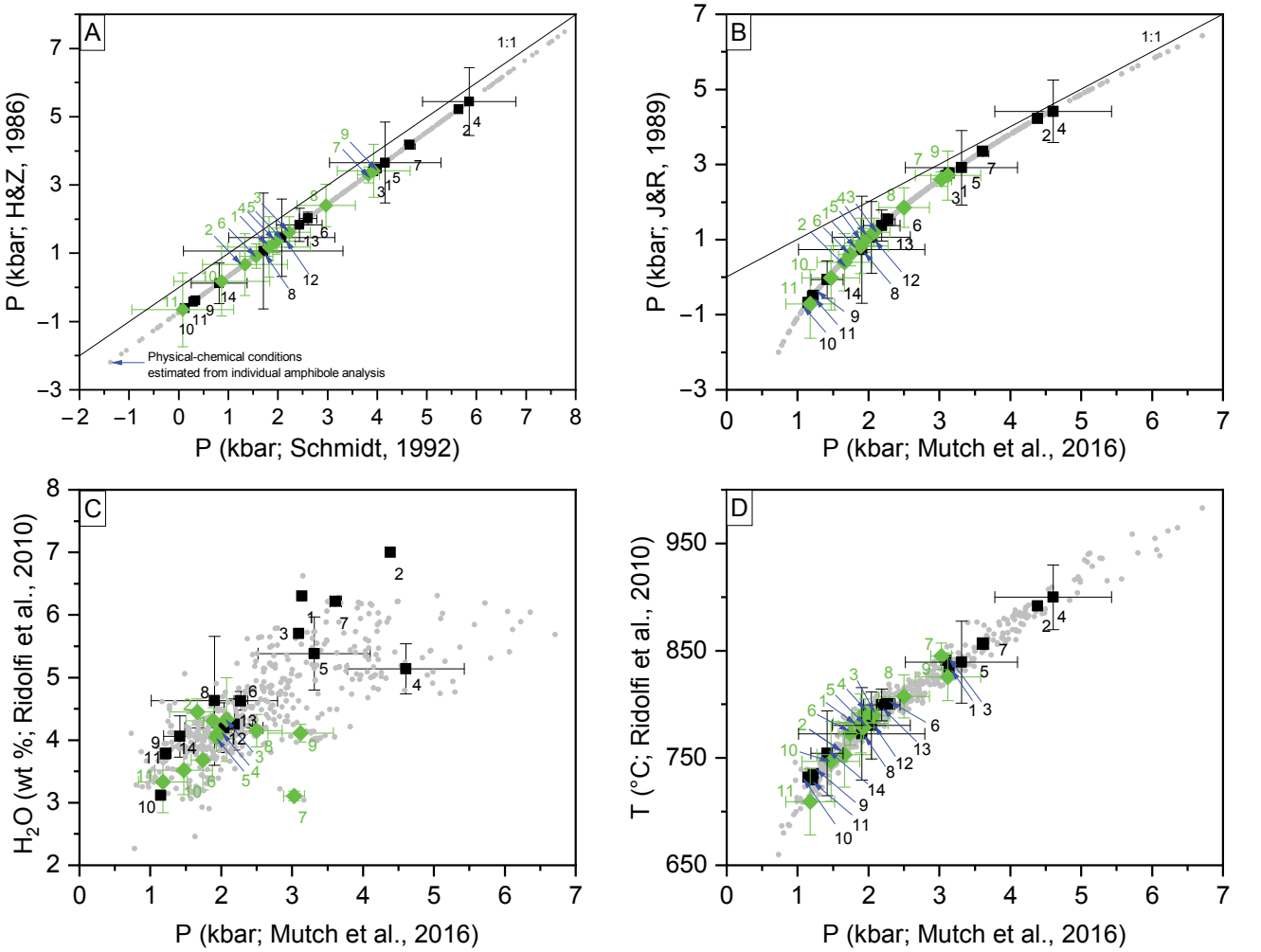

Synsubduction:
1-Santo Tomas II, 2-Clifton, 3-Bumolo, 4-Red Chris, 5-Duolong, 6-Santa Rita, 7-Black Mountain, 8-Xiongcun, 9-Chuquicamata, 10-El Salvador, 11-Rio Blanco, 12-Coroccohuayco, 13-Baogutu, 14-Yerington

Postsubduction:
1-Niutoushan, 2-Fuzishan, 3-Pulang, 4-Ouyangshan, 5-Jiama, 6-Qulong, 7-Yaoan, 8-Yulong, 9-Tongchang, 10-Machangqing, 11-Beiya

Fig. 2. Estimated crystallizing pressures of the amphibole phenocrysts using the barometers of (A) Schmidt (1992) and Hammarstrom and Zen (1986), and (B) Mutch et al. (2016) and Johnson and Rutherford (1989). C) Magmatic H_2O contents vs. amphibole crystallizing pressures. D) Amphibole crystallizing temperatures vs. pressures. Magmatic H_2O contents and amphibole crystallizing temperatures in C and D are calculated using the method of Ridolfi et al. (2010), whereas the amphibole crystallizing pressures are estimated using the method of Mutch et al. (2016). Black and green points with error bars (2 S.D.) represent the average values of the corresponding deposits, which are numbered in Table 1. The gray dots represent individual physical-chemical values of compiled amphibole data (App. Table A1). H&Z (1986) = Hammarstrom and Zen (1986); J&R (1989) = Johnson and Rutherford (1989).

for many compiled deposits (i.e., Santo Tomas II, Clifton, Bumolo, Chuquicamata, El Salvador, Rio Blanco, Yerington; Dilles, 1987; Imai, 2002; Ishihara and Imai, 2014). This prevents us from using the apatite hygrometer. Estimating water content using bulk rock composition is commonly applied to eruptive magmas or melt inclusions (Ghiorso and Gualda, 2015). However, the H_2O content estimated from porphyritic intrusions does not necessarily reflect the H_2O content of the underlying magma reservoir, which is the main source of outgassed fluids in porphyry Cu systems. In addition, the porphyritic intrusions are inevitably affected by hydrothermal alteration, as indicated by high loss-on-ignition values in some deposits (e.g., Yaoan, 0.5–6.25 wt %; Red Chris, 2.33–8.22 wt %; App. Table A3). Given these issues, the bulk rock method is also considered inappropriate to estimate magmatic water content. Thus, we have used the amphibole hygrometer to estimate H_2O contents in the magmatic systems associated with porphyry Cu deposits.

As shown in Figures 2C and 3A-F, magmatic systems associated with subduction-related porphyry Cu deposits have

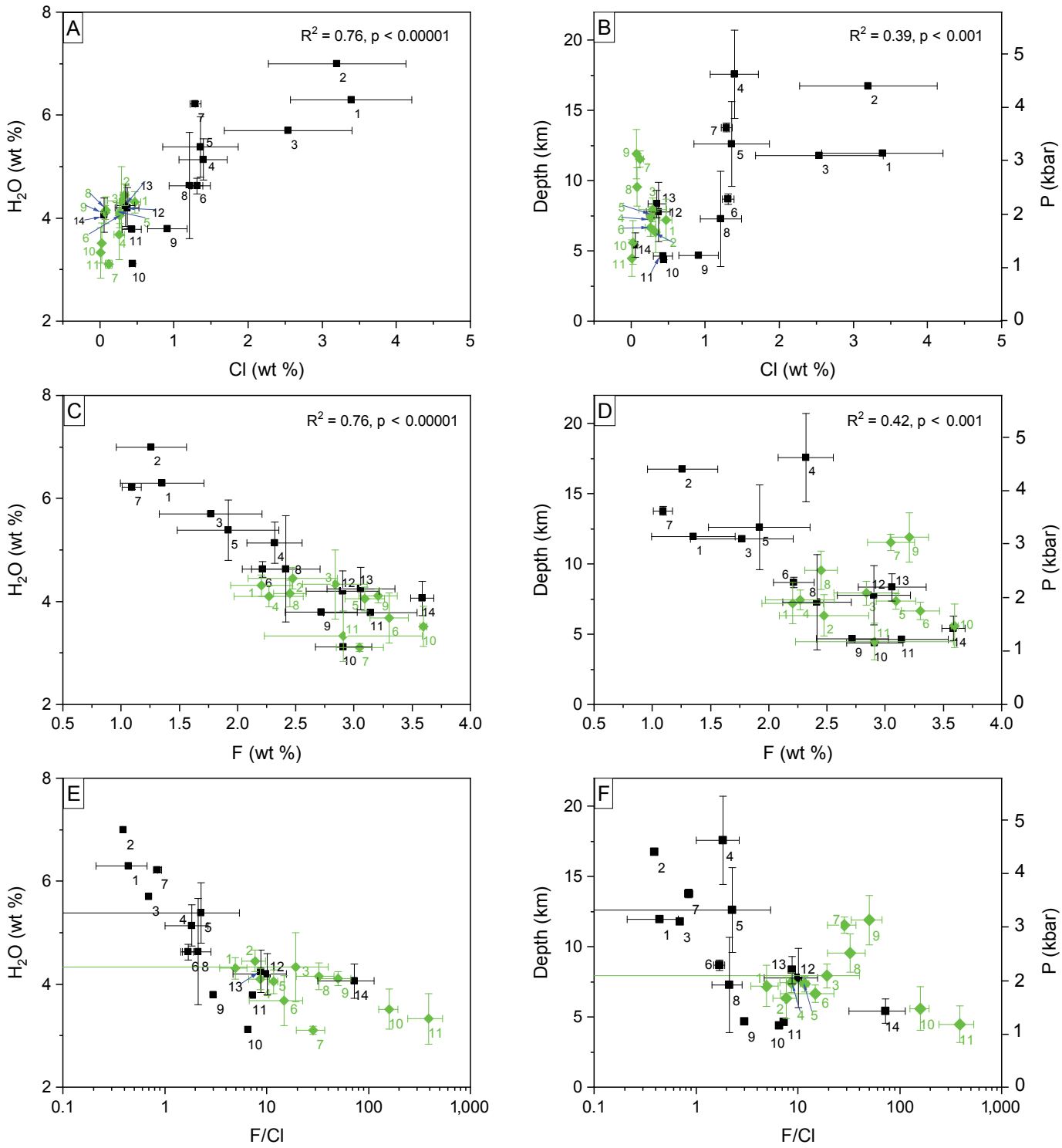

Syn-subduction:

1-Santo Tomas II, 2-Clifton, 3-Bumolo, 4-Red Chris, 5-Duolong, 6-Santa Rita, 7-Black Mountain, 8-Xiongcun, 9-Chuquicamata, 10-El Salvador, 11-Rio Blanco, 12-Coroccohuayco, 13-Baogutu, 14-Yerington

Post-subduction:

1-Niutoushan, 2-Fuzishan, 3-Pulang, 4-Ouyangshan, 5-Jiama, 6-Qulong, 7-Yaoan, 8-Yulong, 9-Tongchang, 10-Machangqing, 11-Beiya

Fig. 3. A-F) Correlations between apatite F and Cl contents and F/Cl ratios, magmatic H_2O contents, and magma reservoir depth. Individual points with error bars (2 S.D.) represent the average values of the corresponding deposits (Fig. 1; Table 1).

water contents ranging from 3.1 wt % (El Salvador, calculated from average amphibole compositions of 24 analyses; Ishihara and Imai, 2014) to 7.0 wt % (Clifton, calculated from average amphibole compositions of four analyses; Imai, 2001), and magma reservoir depths ranging from 4.4 km (El Salvador, calculated from average amphibole compositions of 24 analyses; Ishihara and Imai, 2014) to 18 ± 3 km (n = 51; Red Chris; Zhu et al., 2018). These values are broadly consistent with the magma reservoir depth for porphyry Cu deposits (5–15 km; Cloos, 2001; Sillitoe, 2010; Richards, 2011).

Magmatic water contents and magma reservoir depth of postsubduction porphyry Cu deposits show less variation, ranging from 3.1 ± 0.1 wt % (n = 4; Yao'an; Bi et al., 2009) to 4.5 ± 0.2 wt % (n = 15; Fuzishan; Duan, 2019), and from 4.5 ± 1.3 km (n = 9; Beiya; Bao et al., 2017) to 12 ± 2 km (n = 21; Tongchang; Xu et al., 2023), respectively (Figs. 2C, 3A-F).

Analytical uncertainties associated with electron microprobe analyses of amphibole are rarely reported for the compiled deposits. Ridolfi et al. (2010) showed that the expected analytical and methodological relative uncertainty for H_2O content estimation is ≤15%, whereas the expected uncertainty for temperature is 22°C. The relative uncertainty of the amphibole geobarometer is ≤16% (Mutch et al., 2016). Propagation of these uncertainties translates into relative errors of 1 to 7% for the calculated average H_2O contents, 0 to 2% for temperature estimates, 1 to 11% for pressure, and 1 to 11% for magma reservoir depth (Table 1).

Apatite Compositions and Calculated Mole Fractions of Cl, F, and OH Apatite

Two methods (Piccoli and Candela, 2002; Ketcham, 2015) are currently available to calculate mole fractions of chlorapatite, fluorapatite, and hydroxyapatite (X_{Cl}, X_F, and X_{OH}, respectively) in apatite, which are based on 13O and approximately 26O, respectively. The method of Ketcham (2015) presumes that all stoichiometrically significant components (including at least P_2O_5 and CaO) are measured. However, apatite analyses from several deposits (i.e., Santo Tomas II, Clifton, Bumolo, Chuquicamata, El Salvador, Rio Blanco, Yerington; Dilles, 1987; Imai, 2002; Ishihara and Imai, 2014) only report F and Cl contents and thus cannot be used for the mole fraction calculations using the method of Ketcham (2015). Therefore, we utilize the method of Piccoli and Candela (2002) to calculate apatite X_{Cl}, X_F, and X_{OH} values (App. Table A2). To test the consistency between these two methods, a subset of apatites with measured components similar to those required by Ketcham (2015) (Coroccohuayco and Pulang; Chelle-Michou and Chiaradia, 2017; Cao et al., 2021), or with abnormally high X_{OH} values (Black Mountain; Cao et al., 2018), were used to calculate X_{Cl}, X_F, and X_{OH} values with both methods (App. Table A2). As shown in Figure 4A-C, the two methods return equivalent X_{Cl}, X_F, and X_{OH} values, although the method of Piccoli and Candela (2002) returns slightly higher X_{Cl} values when the X_{Cl} values are high (>0.1). For lower X_{Cl} values, the results are very similar. Average apatite F, Cl, and S contents, as well as calculated X_F, X_{Cl}, and X_{OH} values of each deposit, are reported in Table 1.

Apatites from subduction-related porphyry Cu deposits have highly variable F and Cl contents. The F contents range from 1.09 ± 0.08 wt % (n = 8; Black Mountain; Cao et al., 2018) to 3.59 ± 0.10 wt % (multiple analyses from three samples; Yerington; Dilles, 1987), whereas the Cl contents range from 0.06 ± 0.03 wt % (multiple analyses from three samples; Yerington; Dilles, 1987) to 3.39 ± 0.82 wt % (250 analyses from four samples; Santo Tomas II; Imai, 2002; Fig. 3A-D). The F/Cl ratios range more dramatically from 0.4 (41 analyses from one sample; Clifton; Imai, 2002) to 73 ± 41 (multiple analyses from three samples; Yerington; Dilles, 1987; Fig. 3E-F). Calculated X_{Cl}, X_F, and X_{OH} values range from 0.01 ± 0.00 (multiple analyses from three samples; Yerington; Dilles, 1987) to 0.50 ± 0.121 (250 analyses from four samples; Santo Tomas II; Imai, 2002), from 0.29 ± 0.02 (n = 8; Black Mountain; Cao et al., 2018) to 0.95 ± 0.03 (multiple analyses from three samples; Yerington; Dilles, 1987), and from 0.04 ± 0.03 (multiple analyses from three samples; Yerington; Dilles, 1987) to 0.52 ± 0.03 wt % (n = 8; Black Mountain; Cao et al., 2018), respectively (App. Table A2; Fig. 4D).

In contrast, F and Cl contents of apatites from postsubduction porphyry Cu deposits are much less variable, ranging from 2.20 ± 0.27 wt % (n = 15; Niutoushan; Duan, 2019) to 3.60 ± 0.03 wt % (n = 3; Machangqing; Wang et al., 2013) and from 0.01 ± 0.00 wt % (n = 4; Beiya; Wang et al., 2017) to 0.47 ± 0.08 wt % (n = 15; Niutoushan; Duan, 2019), respectively (Fig. 3A-D). The F/Cl ratios range from 4.9 ± 1.5 (n = 15; Niutoushan; Duan, 2019) to 419 ± 142 (n = 4; Beiya; Wang et al., 2017; Fig. 3E-F). Calculated X_{Cl}, X_F, and X_{OH} values range from 0.001 ± 0.000 (n = 4; Beiya; Wang et al., 2017) to 0.07 ± 0.01 (n = 15; Niutoushan; Duan, 2019; Fig. 3A-D), from 0.59 ± 0.07 (n = 15; Niutoushan; Duan, 2019) to 0.96 ± 0.01 (n = 3; Machangqing; Wang et al., 2013), and from 0.04 ± 0.01 (n = 3; Machangqing; Wang et al., 2013) to 0.36 ± 0.08 wt % (n = 15; Ouyangshan; Duan, 2019), respectively (App. Table A2; Fig. 4D).

The apatite S contents, in contrast to F and Cl contents, are broadly similar between synsubduction (0.03 ± 0.02 wt % of Xiongcun to 0.24 ± 0.19 wt % of Duolong; Xie et al., 2018; Li et al., 2021) and postsubduction (0.04 ± 0.02 wt % of Machangqing to 0.48 ± 0.17 wt % of Beiya; Wang et al., 2017) porphyry Cu deposits (Fig. 5).

Electron microprobe analyses of apatite generally have relative errors of ≤10% for Cl, F, and S contents (e.g., Chelle-Michou and Chiaradia, 2017; Cao et al., 2021). Propagation of these analytical uncertainties translates into small relative errors for calculated average Cl, F, and S contents (1–7%), as well as for X_F and X_{Cl} values (1–6%) and F/Cl ratios (2–9%; Table 1). Relative errors of the calculated X_{OH} are within the range of 2 to 27%, with the exceptions of the Yerington and Machangqing deposits, which have large relative errors of 140 and 132%, respectively. For the Machangqing deposit, the large error is likely due to limited apatite analyses (n = 3). For the Yerington deposit, although multiple analyses were conducted from three samples, only average values of each sample were reported (Dilles, 1987). Propagation of analytical uncertainties from these three averaged values likely led to the large relative error.

Overall, the compiled data show that the apatite Cl contents exhibit positive correlations, whereas the F contents and F/Cl ratios exhibit negative correlations, with both magmatic water contents and magma reservoir depth (Fig. 3A-F). These

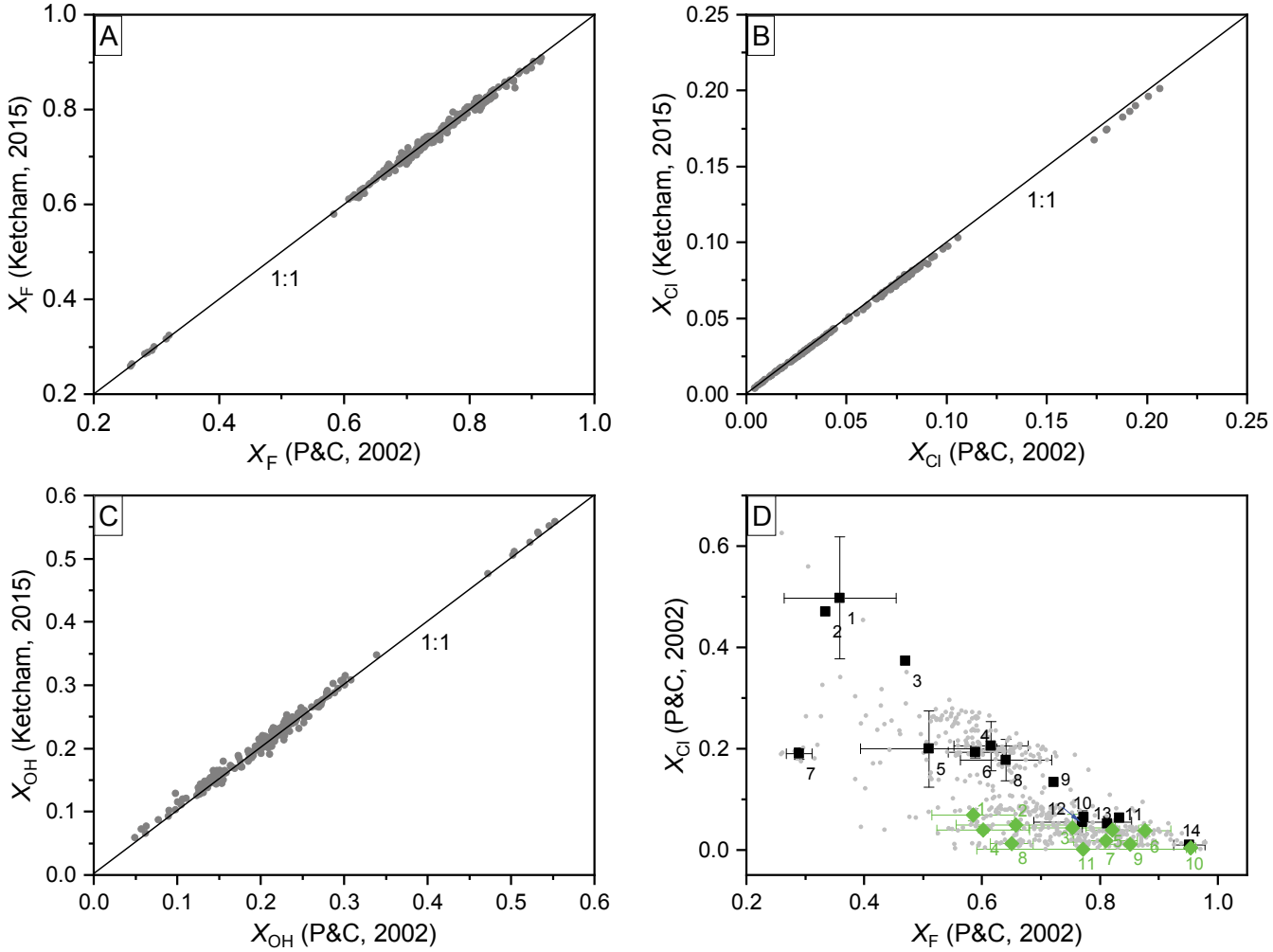

Synsubduction:

1-Santo Tomas II, 2-Clifton, 3-Bumolo, 4-Red Chris, 5-Duolong, 6-Santa Rita, 7-Black Mountain, 8-Xiongcun, 9-Chuquicamata, 10-El Salvador, 11-Rio Blanco, 12-Coroccohuayco, 13-Baogutu, 14-Yerington

Postsubduction:

1-Niutoushan, 2-Fuzishan, 3-Pulang, 4-Ouyangshan, 5-Jiama, 6-Qulong, 7-Yaoan, 8-Yulong, 9-Tongchang, 10-Machangqing, 11-Beiya

Fig. 4. Estimated X_F (A), X_{Cl} (B), and X_{OH} (C) values of a subset of apatites (from the Coroccohuayco, Pulang, and Black Mountain deposits) using the methods of Piccoli and Candela (2002) and Ketcham (2015). D) Correlation between apatite X_F and X_{Cl} values of the compiled deposits. Black and green points with error bars (2 S.D.) in (D) represent the average values of the corresponding deposits (Table 1), whereas the gray dots represent individual physical-chemical values of compiled apatite data (App. Table A2). P&C (2002) = Piccoli and Candela (2002).

trends also hold true when plotting all three volatile members (i.e., X_{Cl}, X_F, and X_{OH}) on a ternary diagram, which shows decreasing X_{Cl} and X_{OH} but increasing X_F, with decreasing water contents and pressure (Fig. 6A-B).

Discussion

Evaluation of potential effects of primary magmatic F-Cl contents, temperature, and postcrystallization diffusion and alteration on apatite F-Cl contents

Apatite F and Cl contents are potentially controlled by four key factors: (1) the primary magmatic F and Cl contents (Zhu et al., 2018); (2) the temperature-dependent exchange coefficients (K_D) of volatile pairs (i.e., OH-F, Cl-F, and OH-Cl) between apatite and silicate melt (Li and Herman, 2017; Li and Costa, 2020); (3) the postcrystallization diffusive reequilibration and/or hydrothermal alteration (Bouzari et al., 2016; Li et al., 2020); and (4) the relative timing between apatite crystallization and magma degassing or fluid exsolution (Stock et al., 2018). During degassing, Cl is preferentially partitioned into the exsolving aqueous fluids, whereas F is preferentially retained in the melt, leading to increasing X_F/X_{Cl} (and F/Cl) but decreasing X_{Cl}/X_{OH} ratios in the apatite crystallized

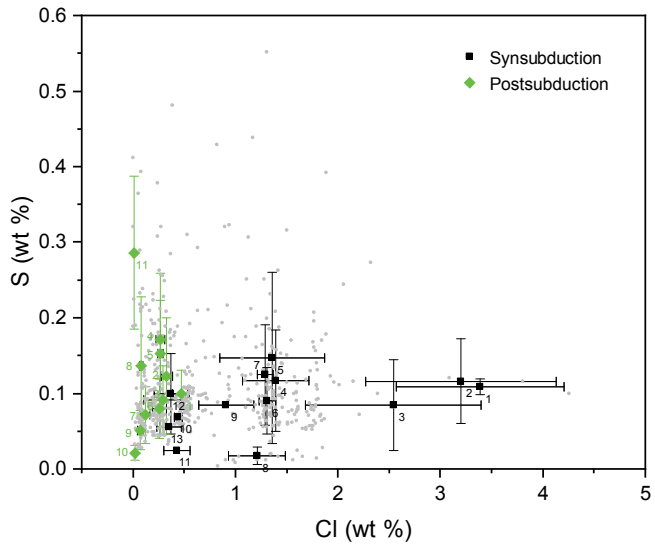

Fig. 5. Apatite Cl contents vs. S contents. Black and green points with error bars (2 S.D.) represent the average values of the corresponding deposits (Table 1), whereas the gray dots represent individual physical-chemical values of compiled apatite data (App. Table A2). The numbers and names of the deposits are listed in Table 1.

afterwards (e.g., $D_{Cl}^{fluid/melt}$ = 16–115 in felsic systems at 200 MPa and 900°–924°C, Webster et al., 2009; $D_{F}^{fluid/melt}$ = 0.13–0.37 in felsic systems at 200 MPa and 775°–994°C, Borodulin et al., 2009).

Low primary magmatic Cl contents are considered unlikely to be the real cause of low-Cl apatite in porphyry Cu systems, particularly those from postsubduction settings (e.g., Yulong, and Qulong; Fig. 3A-B), as suggested by the following lines of evidence. First, Cl is of critical importance for metal extraction and transportation in an aqueous fluid. For example, Tattitch et al. (2021) demonstrated that increasing melt Cl concentration at fluid saturation from 500 to 3,000 ppm leads to almost eightfold increase in Cu extraction efficiency. Thereby, the giant sizes of some porphyry Cu deposits, which have low-Cl apatites (<0.3 wt % Cl; e.g., 11 Mt Cu at Qulong, 6.2 Mt Cu at Yulong; Yang and Cooke, 2019), logically require sufficiently high magmatic Cl contents to extract and transport the metals into the exsolved aqueous fluid. Second, apatites from premineralization intrusions have systematically higher Cl contents than low-Cl apatites of the synmineralization intrusions (e.g., Yerington, Yulong, and Coroccohuayco; Dilles, 1987; Chelle-Michou and Chiaradia, 2017; Huang et al., 2019). This indicates that primary magmatic Cl contents of these systems, although likely to be variable (Webster et al., 2018), are probably higher than those recorded by apatites in the synmineralization intrusions.

Temperature differences among deposits, as inferred by the geothermometry of hosting amphibole (Fig. 2D), could affect the exchange coefficient of volatile pairs between apatite and melt and lead to variable apatite volatile contents (Li and Herman, 2017; Li and Costa, 2020). Nonetheless, Li and Costa (2020) also showed that the exchange coefficient (particularly for the Cl-F pair) shows a greater dependence on apatite composition than on temperature. McCubbin et al. (2015) further demonstrated that the apatite-melt exchange coefficient would remain constant for apatite with X_F > 0.18. Given the high X_F values of the apatites of our database (all >0.25; Fig. 4D), we expect that temperature differences have minimal effects on exchange coefficient and thereby on apatite volatile variabilities among deposits.

Postcrystallization diffusive homogenization and/or reequilibration are also unlikely to be responsible for the highly variable apatite volatile contents among deposits, as argued below. Before being enclosed in silicate phenocrysts, the apatite volatile record is likely in equilibrium with the melt, because diffusive equilibration is reached rapidly, within 3.7 to 140 days for apatite crystals 90 µm in diameter, under magmatic temperatures (700°–900°C; Humphreys et al., 2021). After being enclosed in silicate phenocrysts, the apatite volatile record should be sheltered from reequilibration with hydrothermal fluids. Indeed, multiple analyses on single apatite grains enclosed by silicate minerals from many of our compiled deposits show homogeneous F and Cl contents (e.g., Yerington, Yulong, Red Chris, Pulang; Streck and Dilles, 1998; Zhu et al., 2018; Cao et al., 2021; Huang et al., 2022), which could indicate negligible F-Cl diffusion in apatite and therefore preservation of magmatic volatile contents. Alternatively, the homogeneous volatile contents in these apatites could be the result of a complete subsolidus reequilibration. To evaluate which one of these two scenarios is the most likely, we calculated the timescales required for complete Cl, F, and OH diffusion equilibration for a spherical particle of radius r. To calculate the time scales, we have used the equation r ≈ sqrt(4Dt), where D is the diffusion coefficient and t is the time taken for 95% of net chemical exchange toward complete equilibration (Crank, 1975). Assuming diffusion parallel to the c-axis (diffusion coefficient D calculated from Li et al., 2020) at a temperature of 550°C (typical of high-temperature hydrothermal alteration; Audétat, 2019) and apatite length of 100 µm (i.e., r = 50 µm), the time scales for complete diffusion of Cl, F, and OH are 1.3, 1.4, and >100 Ma, respectively. Given that Cl and OH diffusion parallel to a-axis is one to two orders of magnitude slower than that parallel to the c-axis (Li et al., 2020), the above results are likely minimum values. Since the lifespans of hydrothermal events (normally tens of k.y.; e.g., Li et al., 2017; Large et al., 2021) are significantly shorter than the above diffusion timescales, we consider that the apatite should preserve the melt volatile information when shielded in silicate phenocrysts.

In addition, Bouzari et al. (2016) showed that apatite chemical compositions, particularly Mn/Fe, Na, and to a lesser extent, Mn contents, can be used to identify hydrothermal alteration related to porphyry copper deposits. Given that different apatite Mn contents among deposits may simply reflect the differences in the melt compositions (Sha and Chappell, 1999; Zirner et al., 2015; Bouzari et al., 2016; Marks et al., 2016) rather than being caused by hydrothermal alteration, we restrict our discussion to the more reliable Mn/Fe ratios and Na contents where these data are available (Bouzari et al., 2016). No correlation between apatite Cl contents and Mn/Fe ratios or Na contents is observed (App. Fig. A2), indicating minimal effects of hydrothermal alteration on apatite Cl contents. Therefore, postentrapment diffusion or hydrothermal alteration are unlikely to reset the volatile record of apatite included in silicate minerals and cannot be

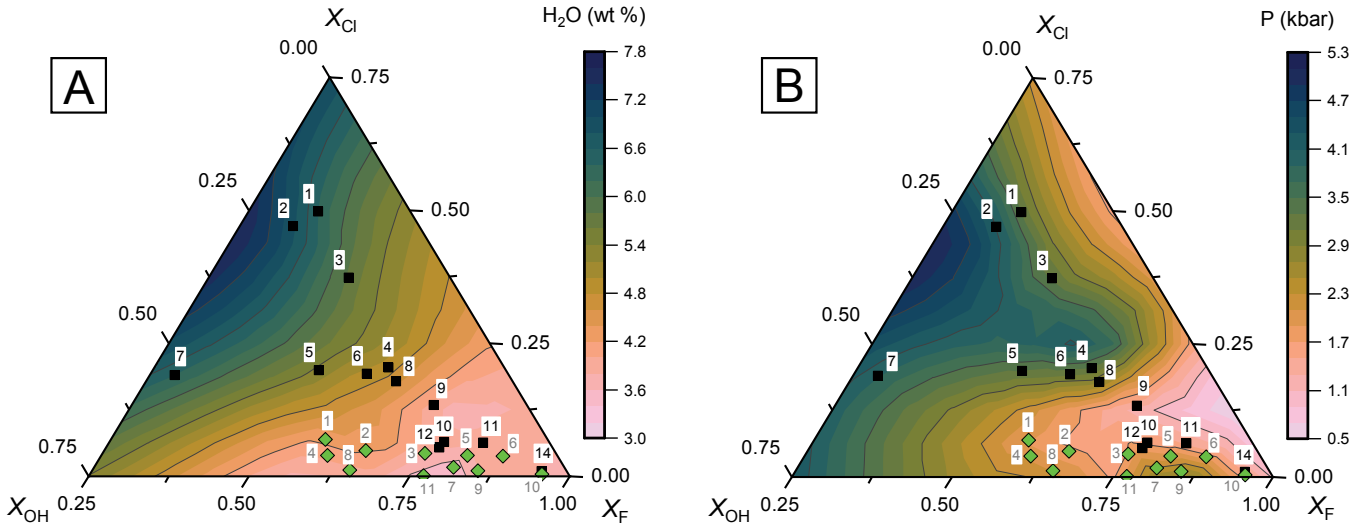

Synsubduction:
1-Santo Tomas II, 2-Clifton, 3-Bumolo, 4-Red Chris, 5-Duolong, 6-Santa Rita, 7-Black Mountain, 8-Xiongcun, 9-Chuquicamata, 10-El Salvador, 11-Rio Blanco, 12-Coroccohuayco, 13-Baogutu, 14-Yerington

Postsubduction:
1-Niutoushan, 2-Fuzishan, 3-Pulang, 4-Ouyangshan, 5-Jiama, 6-Qulong, 7-Yaoan, 8-Yulong, 9-Tongchang, 10-Machangqing, 11-Beiya

Fig. 6. Ternary plots of the volatile contents in apatite (in molar proportions) compiled in this study contoured as a function of (A) water contents estimated based on amphibole composition (Ridolfi et al., 2010) and (B) pressures of the magma reservoirs estimated with the Al-in-amphibole barometer of Mutch et al. (2016). Note that there is a general trend of decreasing X_{Cl} and X_{OH}, but increasing X_F, with decreasing water contents and pressure.

responsible for the highly variable apatite volatile contents among the investigated deposits.

Apatite F-Cl contents of porphyry Cu deposits controlled by depth-related fluid exsolution processes

We argue that the variability of apatite Cl and F contents among deposits most likely reflects variable melt Cl and F contents at the time of apatite crystallization, which is controlled by the relative timing of fluid exsolution and apatite saturation in originally Cl-rich magmas (> ~3,000 ppm Cl; Webster et al., 2018; Tattitch et al., 2021). Ore-forming fluids, together with their volatile and metal cargo, are outgassed from underlying magma reservoirs upon hydraulic fracturing of the magmatic carapace, which is caused by the buildup of magmatic fluid pressure during magma fractional crystallization (Burnham, 1979; Richards, 2011). Fluid exsolution may lead to Cl depletion but F enrichment in the residual melt due to contrasted fluid/melt partition behavior of Cl and F. Although exsolution of F- and Cl-bearing fluids may not happen if the melt F-Cl contents are too low, this does not apply to intermediate-felsic arc-related magmas, which are known to be rich in these and other volatiles. In addition, it has been shown that parental magmas of postsubduction, shallower porphyry Cu systems are as hydrous as those of the synsubduction, deeper systems (Lu et al., 2015; Chiaradia, 2020b). Water solubility in silicate melts strongly increases with increasing pressure (Newman and Lowenstern, 2002). Therefore, deeper magma reservoirs require more extensive crystallization to reach fluid exsolution and ultimately form a porphyry Cu deposit (Cline and Bodnar, 1991). In addition, the higher H_2O contents of the deeper magma reservoirs (Fig. 3A-F) may delay magma crystallization, thus these more hydrous magmas would require greater degree of cooling to crystallize and achieve fluid saturation (Caricchi and Blundy, 2015). In these deep reservoirs, apatite may crystallize prior to extensive fluid exsolution and Cl loss, thus having relatively high Cl contents and low F/Cl ratios. By contrast, fluid exsolution may occur at relatively early stages of differentiation in shallower reservoirs associated with porphyry Cu systems due to the lower magmatic H_2O solubility at lower pressure. In these systems, apatite may crystallize after fluid exsolution from a melt enriched in F but depleted in Cl because of the higher partitioning of Cl into the exsolved aqueous fluid. Due to the competing behavior of F and Cl when partitioning into apatite, the apatite crystallized after fluid exsolution would have relatively high F but low Cl contents and therefore high F/Cl ratios. Although the crystallization-driven fluid exsolution (second boiling) has been recently suggested to result in an initial increase (and then drop) of the melt Cl content (Tattitch et al., 2021), the melt F/Cl ratio would keep increasing due to the contrasting fluid/melt partitioning behavior of Cl and F. The elevated melt F/Cl ratio may also result in lower Cl but higher F contents and thereby higher F/Cl ratios of the apatite crystallized after fluid exsolution due to the competing relationships of F and Cl when partitioning into apatite.

The above interpretation is also supported by the common occurrence of fluid inclusions in apatite from shallowly emplaced postsubduction porphyry Cu systems in the Tibetan Plateau (i.e., Yulong, Qulong, Jiama; Fig. 7A-F). These fluid

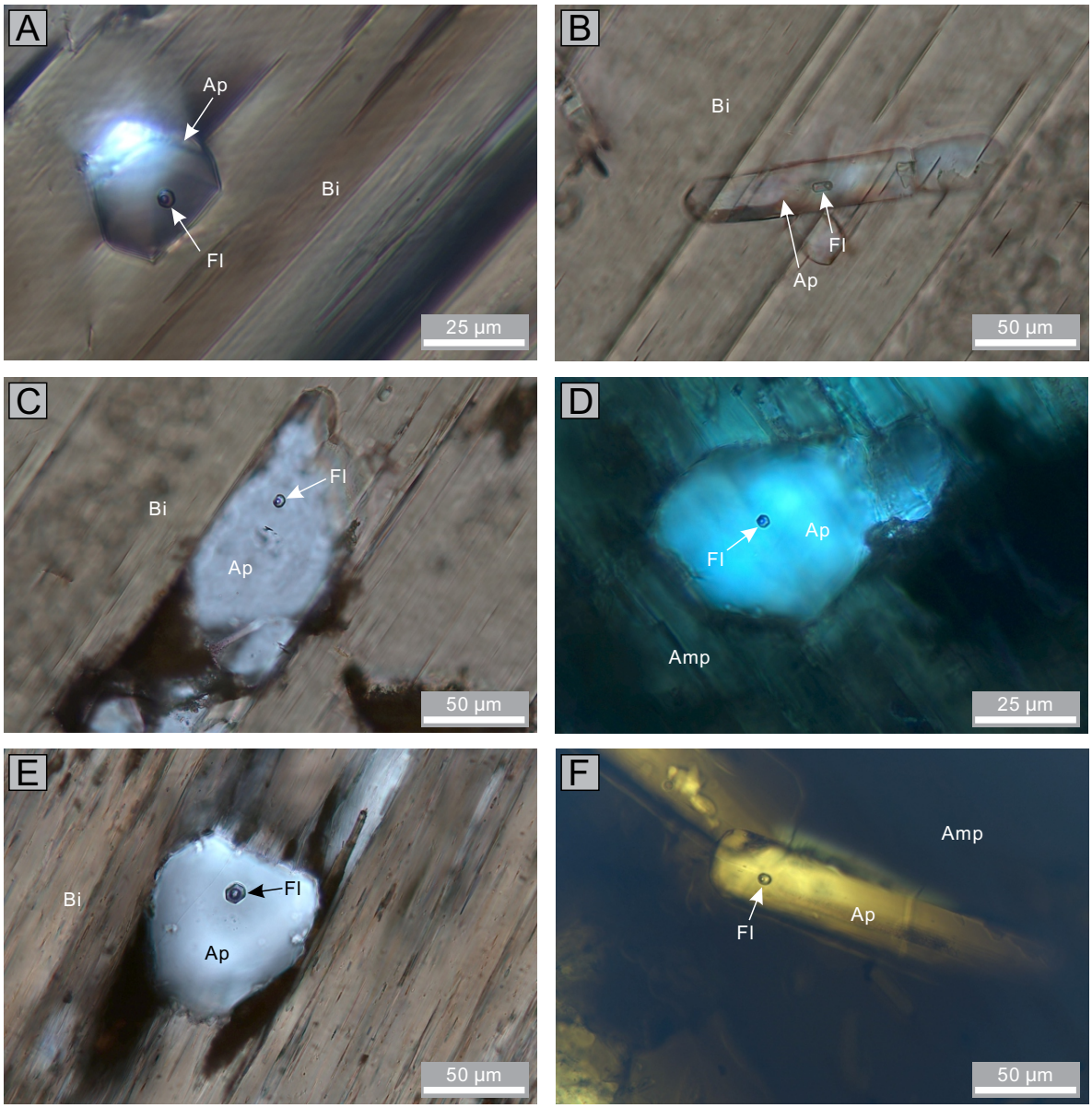

Fig. 7. Representative apatite-hosted ID-type fluid inclusions (Fl) in the Yulong deposit from the Yulong belt of eastern Tibet (A-D), and the Qulong (E) and Jiama (F) porphyry Cu-Mo deposits from the Gangdese belt of southern Tibet. (A) is taken from sample YL1652, which was collected from the Yulong mining pit. (B) and (C) are taken from the sample collected from 671 m depth of drill hole ZK1007. (D) is taken from the sample collected from 810 m depth of drill hole ZK1007. (E) is taken from sample QL1521 that was collected from the Qulong mining pit. (F) is taken from sample 18JM-79 that was collected from 474 m depth of drill hole ZK2015. Abbreviations: Amp = amphibole, Ap = apatite, Bi = biotite.

inclusions are contained in apatite that is enclosed in fresh silicate phenocrysts (e.g., amphibole and biotite) and are considered to have a primary origin based on petrographic observations. They all consist of an aqueous liquid phase of 40 to 70 vol % and a vapor bubble of 30 to 60 vol %, similar to initial single-phase intermediate-density (ID type) fluid inclusions commonly observed in porphyry Cu systems (e.g., Landtwing et al., 2010; Audétat, 2019). In contrast, similar cases have not been reported in high-Cl apatite from deep porphyry Cu systems (e.g., Red Chris and Santo Tomas II; Imai, 2002; Zhu et al., 2018). This indicates that fluid exsolution has likely occurred before or during apatite crystallization in shallowly emplaced systems and is probably responsible for the remarkable variability of apatite Cl and F contents among porphyry Cu systems.

Possible causes of different magma reservoir depths between syn- and postsubduction porphyry deposits and implications for ore-forming processes

The data presented above show that synsubduction and postsubduction porphyry Cu systems have distinct features in terms of apatite Cl and F contents, which are interpreted to result from different magma reservoir depths. A key question is what controls the different magma reservoir depths of syn-

and postsubduction porphyry Cu systems. We speculate that these differences could result from distinct tectonic regimes in syn- and postsubduction settings, as explained below. Already, Chiaradia (2020a) has argued for different evolution depths of magmatic systems associated with syn- and postsubduction porphyry Cu-Au deposits based on distinct Sr/Y compositions of the magmas.

Compressional settings and tectonic regime changes play an important role in the formation of subduction-related porphyry Cu deposits (Sillitoe, 1998; Tosdal and Richards, 2001; Cooke et al., 2005; Richards et al., 2011; Loucks, 2014). Sillitoe (1998) proposed that compression on the overriding plate, which likely results from low-angle subduction (slab flattening) of aseismic ridges, seamount chains, or oceanic plateaus (Cooke et al., 2005), would slow down magma ascent through the crust, aid the development of large lower- to midcrustal magma reservoirs, and promote magma evolution at deep to intermediate crustal levels (see also Chiaradia and Caricchi, 2017). Magmatic systems so formed are vertically extensive and are H_2O-rich due to the variably high-pressure fractionation of mantle-derived hydrous magmas (Cashman et al., 2017; Melekhova et al., 2017; Journeau et al., 2022). Despite high H_2O contents (up to >10 wt %), however, most of these evolved magmas are H_2O-undersaturated at high pressure (Chiaradia and Caricchi, 2017). Relaxation of crustal stress associated with changes in the tectonic regime after the long compression periods allows the ascent of magmas to shallower levels where fluids can be exsolved and form porphyry Cu deposits (Tosdal and Richards, 2001). In these systems, it is possible that significant amounts of apatite crystallize at depths before magma ascent to a shallower level, where it may exsolve an aqueous fluid. Therefore, these apatites will keep a higher-pressure predegassing record of magmatic volatile contents. For some synsubduction deposits, low-Cl apatites seem to indicate crystallization in a shallow magma reservoir compared to most of the synsubduction porphyry Cu deposits. This requires further investigation to understand whether these deposits are characterized by more complex transcrustal magmatic systems with the development of shallower magma chambers than in most of the other synsubduction porphyry Cu deposits.

In contrast, postsubduction porphyry Cu deposits have been suggested to be formed in relatively extensional settings (Hou et al., 2004; Richards, 2009; Zheng et al., 2019; Chiaradia, 2020a). For instance, based on the close spatial-temporal association among ore-forming intrusions, potassic-ultrapotassic lavas, and regional north-south normal faults, Hou et al. (2004) demonstrated that postsubduction porphyry Cu deposits in the Gangdese belt of southern Tibet were formed under extensional conditions. Similar conclusions have been reached for the Yulong and Ailaoshan-Red River belt, southwest China (Chung et al., 1997; Hou et al., 2003), and for the Middle-Lower Yangtze River belt, east China (Zhou et al., 2015). An extensional setting may allow rapid ascent and emplacement of hydrous magmas in shallow reservoirs, short-circuiting the vertical transcrustal magmatic system typically associated with long periods of compression in synsubduction settings. In the shallow reservoir, the hydrous magma may exsolve fluids already at early stages of differentiation, e.g., before apatite crystallization, because of the pressure dependency of H_2O solubility in silicate melt. Apatites crystallized from these magmas will mostly keep a shallow postdegassing record of magmatic volatile contents. The occurrence of primary fluid inclusions in phenocryst-hosted apatites from shallow porphyry Cu systems (Fig. 7A-F) supports that initial fluid exsolution has occurred at early stages of magma evolution. These apatite-hosted fluid inclusions, which may represent discrete aliquots of fluid released from different portions of the system (Tattitch et al., 2021), could have preserved pristine physical-chemical properties of initial ore-forming fluids, which are traditionally obtained by fluid inclusions in quartz veins or unidirectional solidification textures (USTs; e.g., Audétat, 2019). Future systematic study of these apatite-hosted fluid inclusions may shed new light on magmatic-hydrothermal transition and hydrothermal evolution in porphyry Cu systems.

Implication for exploration

The global scale correlation between apatite F and Cl contents and depths of magma reservoirs associated with porphyry Cu deposits has important implications for the usage of apatite as a potential fertility tracer. In fact, apatite Cl and F contents do not necessarily reflect the primary chemical signature of their parental magma. This conclusion also applies to some fluid-mobile trace elements such as Sr, whose contents may also be controlled by the relative timing of fluid saturation and apatite crystallization. Therefore, they may be inappropriate as a porphyry Cu fertility indicator, unless it is shown that the studied apatites are early crystallizing phases (e.g., Nathwani et al., 2020) that are not affected by fluid exsolution processes. This implication is very important because apatite compositions (e.g., Cl contents and Sr/Y ratios) have been increasingly used to discriminate porphyry Cu related intrusions from barren intrusions, and from intrusions associated with W-Mo and/or Pb-Zn deposits (e.g., Mao et al., 2016; Pan et al., 2016; Zhong et al., 2018; Zafar et al., 2019; Xing et al., 2020; Cao et al., 2021). While agreeing with previous studies that high magmatic Cl contents favor porphyry Cu formation (e.g., Cline and Bodnar, 1991; Imai, 2002; Ishihara and Imai, 2014; Zhu et al., 2018; Tattitch et al., 2021), we argue that it is the primary magmatic Cl contents of a magmatic system, rather than those estimated from apatite Cl contents, that may be used to evaluate its porphyry Cu fertility. Measured Cl contents of apatite are not necessarily representative of the original melt Cl contents. Low Cl contents measured in apatite and estimated in melt may be simply diagnostic of early fluid exsolution and do not necessarily indicate low Cu potential.

On the other hand, apatite sulfur contents largely overlap among syn- and postsubduction porphyry Cu deposits (Fig. 5) and are mostly relatively high (>0.05 wt %) compared to more reduced and infertile magmas (<0.05 wt %; e.g., Ishihara and Imai, 2014; Richards et al., 2017; Zhu et al., 2022). In addition, within individual porphyry Cu systems, the apatite S content is much less variable than Cl and largely remains high during magma evolution and fluid exsolution, as has been shown in several porphyry Cu systems (e.g., Coroccohuayco, Chelle-Michou and Chiaradia, 2017; Duolong, Li et al., 2021; Yulong, Huang et al., 2022). This could be interpreted to be the result of buffering of early-saturated sulfate in oxidized and sulfur-

rich magmas (Hutchinson and Dilles, 2019), a possibility supported by the common observation of anhydrite in many of the compiled deposits (i.e., El Salvador and Yerington, Hutchinson and Dilles, 2019; Duolong, Li et al., 2021; Yulong, Chang et al., 2018; Qulong, Xiao et al., 2012). These magmatic anhydrites may break down during fluid exsolution and thus constitute an important sulfur source to mineralizing fluids (Streck and Dilles, 1998; Grondahl and Zajacz, 2017; Hutchinson and Dilles, 2019; Li et al., 2021). Therefore, high apatite S content might be a robust proxy for relatively oxidized nature of the parental magma, and therefore useful to discriminate oxidized, S-rich magmas from the relatively reduced, S-poor infertile magmas.

Conclusions

Apatite and amphibole compositions from 25 porphyry Cu deposits worldwide have been compiled. The amphibole compositions were used to calculate magmatic water contents and crystallization pressure, a proxy of magma reservoir depth. We find that the apatite Cl contents show positive correlations, whereas the F contents and F/Cl ratios show negative correlations, with both magmatic water contents and magma reservoir depth. Postsubduction porphyry Cu deposits are associated with overall shallower magma reservoirs and lower apatite Cl contents than the great majority of synsubduction porphyry Cu deposits. Combined with the common occurrence of primary intermediate-density fluid inclusions in apatite from shallower postsubduction porphyry Cu systems, we interpret these correlations as reflecting early fluid exsolution and associated magmatic Cl loss that predate apatite crystallization in shallow porphyry Cu systems. In contrast, in magmatic systems associated with synsubduction porphyry Cu deposits, the Cl and F systematics suggest that apatites have mostly crystallized prior to fluid exsolution. The apatite S contents are broadly similar for all deposits, implying that they are not affected by fluid exsolution. This is probably due to the buffering effect of early-saturated sulfate in oxidized and sulfur-rich magmas. Therefore, apatite sulfur contents might be a better fertility indicator than apatite Cl contents. It is speculated that postsubduction porphyry Cu deposits are associated with shallower magma reservoirs owing to their formation in relatively extensional tectonic regimes. Our results argue that fluid exsolution and associated magmatic Cl loss may occur early in shallow porphyry systems. Systematic studies of apatite-hosted fluid inclusions may shed new light on the magmatic-hydrothermal transition and hydrothermal evolution in these shallow porphyry Cu systems.

Acknowledgments

We thank Editor-in-Chief Larry Meinert and an editorial board member for handling the manuscript. Weiran Li and Chetan Nathwani are acknowledged for their constructive reviews, which helped to improve our work significantly. The authors would also like to thank Jian-Feng Gao from the Institute of Geochemistry, Chinese Academy of Sciences, Chusi Li of Indiana University, and Gui-Qing Xie from the Chinese Academy of Geological Sciences for their valuable suggestions on the early version of the manuscript. Shi-Ji Zheng is thanked for the sample from the Jiama deposit. The Scientific color map, batlow (Crameri, 2018), is used in this study to prevent visual distortion of the data and exclusion of readers with color-vision deficiencies (Crameri et al., 2020). This study was funded by the National Natural Science Foundation of China (91955209, 42003038, 41873052).

REFERENCES

Anderson, J.L., and Smith, D.R., 1995, The effects of temperature and fo_2 on the Al-in-hornblende barometer: American Mineralogist, v. 80, p. 549–559.

Audétat, A., 2019, The metal content of magmatic-hydrothermal fluids and its relationship to mineralization potential: Economic Geology, v. 114, p. 1033–1056.

Baldwin, J.A., and Pearce, J.A., 1982, Discrimination of productive and nonproductive porphyritic intrusions in the Chilean Andes: Economic Geology, v. 77, p. 664–674.

Bao, X.S., He, W.Y., and Gao, X., 2017, The Beiya gold deposit: Constraints from water-rich magmas to mineralization: Acta Petrologica Sinica, v. 33, p. 2175–2188 (in Chinese).

Bi, X.W., Hu, R.Z., Peng, J.T., Wu, K.X., Su, W.C., and Zhang, X.Z., 2005, Geochemcial characteristics of the Yao'an and Machangqing alkaline-rich intrusions: Acta Petrologica Sinica, v. 21, p. 113–124 (in Chinese with English abs.).

Bi, X.W., Hu, R.Z., Hanley, J.J., Mungall, J.E., Peng, J.T., Shang, L.B., Wu, K.X., Suang, Y., Li, H.L., and Hu, X.Y., 2009, Crystallization conditions (T, P, fo_2) from mineral chemistry of Cu- and Au-mineralized alkaline intrusions in the Red River-Jinshajiang alkaline igneous belt, western Yunnan province, China: Mineralogy and Petrology, v. 96, p. 43–58.

Borisova, A.Y., Pichavant, M., Beny, J.M., Rouer, O., and Pronost, J., 2005, Constraints on dacite magma degassing and regime of the June 15, 1991, climactic eruption of Mount Pinatubo (Philippines): New data on melt and crystal inclusions in quartz: Journal of Volcanology and Geothermal Research, v. 145, p. 35–67.

Borodulin, G.P., Chevychelov, V.Yu., and Zaraysky, G.P., 2009, Experimental study of partitioning of tantalum, niobium, manganese, and fluorine between aqueous fluoride fluid and granitic and alkaline melts: Doklady Earth Sciences, v. 427, p. 868–873.

Bouzari, F., Hart, C.J., Bissig, T., and Barker, S., 2016, Hydrothermal alteration revealed by apatite luminescence and chemistry: A potential indicator mineral for exploring covered porphyry copper deposits: Economic Geology, v. 111, p. 1397–1410.

Burnham, C.W., 1979, Magmas and hydrothermal fluids, *in* Barnes, H.L., ed., Geochemistry of hydrothermal ore deposits, 2nd ed.: John Wiley and Sons, New York, p. 71–136.

Cao, K., Yang, Z.M., White, N.C., and Hou, Z.Q., 2021, Generation of the Giant Porphyry Cu-Au deposit by repeated recharge of mafic magmas at Pulang in Eastern Tibet: Economic Geology, v. 117, p. 57–90.

Cao, M.J., Hollings, P., Cooke, D.R., Evans, N.J., McInnes, B.I.A., Qin, K.Z., Li, G.M., Sweet, G., and Baker, M., 2018, Physicochemical processes in the magma reservoir under the Black Mountain porphyry Cu-Au deposit, Philippines: Insights from mineral chemistry and implications for mineralization: Economic Geology, v. 113, p. 63–82.

Caricchi, L., and Blundy, J., 2015, Experimental petrology of monotonous intermediate magmas: Geological Society, London, Special Publications, v. 422, doi: 10.1144/SP422.9.

Cashman, K.V., Sparks, R.S.J., and Blundy, J.D., 2017, Vertically extensive and unstable magmatic systems: A unified view of igneous processes: Science, v. 355, eaag3055.

Chang, J., Li, J.W., and Audétat, A., 2018, Formation and evolution of multistage magmatic-hydrothermal fluids at the Yulong porphyry Cu-Mo deposit, eastern Tibet: Insights from LA-ICP-MS analysis of fluid inclusions: Geochimica et Cosmochimica Acta, v. 232, p. 181–205.

Chelle-Michou, C., and Chiaradia, M., 2017, Amphibole and apatite insights into the evolution and mass balance of Cl and S in magmas associated with porphyry copper deposits: Contributions to Mineralogy and Petrology, v. 172, p. 105.

Chelle-Michou, C., Chiaradia, M., Béguelin, P., and Ulianov, A., 2015, Petrological evolution of the magmatic suite associated with the Coroccohuayco Cu(-Au-Fe) porphyry-skarn deposit, Peru: Journal of Petrology, v. 56, p. 1829–1862.

Chiaradia, M., 2020a, Gold endowments of porphyry deposits controlled by precipitation efficiency: Nature Communications, https://doi.org/10.1038/s41467-019-14113-1.

——2020b, How much water in basaltic melts parental to porphyry copper deposits?: Frontiers in Earth Science, v. 8, p. 138, doi: 10.3389/feart.2020.00138.

Chiaradia, M., and Caricchi, L., 2017, Stochastic modelling of deep magmatic controls on porphyry copper deposit endowment: Scientific Reports, v. 7, article 44523.

Chung, S.L., Lee, T.Y., Lo, C.H., Wang, P.L., Chen, C.Y., Nguyen, T.Y., Tran, T.H., and Wu, G., 1997, Intraplate extension prior to continental extrusion along the Ailao Shan-Red River shear zone: Geology, v. 25, p. 311–314.

Cline, J.S., and Bodnar, R.J., 1991, Can economic porphyry copper mineralization be generated by a typical calc-alkaline melt?: Journal of Geophysical Research, v. 96, p. 8113–8126.

Cloos, M., 2001, Bubbling magma reservoirs, cupolas, and porphyry copper deposits: International Geology Review, v. 43, p. 285–311.

Cooke, D.R., Hollings, P., and Walshe, J.L., 2005, Giant porphyry deposits: Characteristics, distribution, and tectonic controls: Economic Geology, v. 100, p. 801–818.

Crameri, F., 2018, Scientific colour maps: Zenodo, doi: 10.5281/zenodo.1243862.

Crameri, F., Shephard, G.E., and Heron, P.J., 2020, The misuse of colour in science communication: Nature Communications, v. 11, article 5444, doi: 10.1038/s41467-020-19160-7.

Crank, J., 1975, The mathematics of diffusion, 2nd ed.: London, Oxford University Press, 145 p.

Dilles, J., 1987, Petrology of the Yerington batholith, Nevada: Evidence for evolution of porphyry copper ore fluids: Economic Geology, v. 82, p. 1750–1789.

Duan, D.F., 2019, Geological character and ore genesis of Cu-polymetallic deposits surrounding Yangxin batholith: Ph.D. thesis, Wuhan, China, China University of Geosciences, 264 p.

Erdmann, S., Martel, C., Pichavant, M., and Kushnir, A., 2014, Amphibole as an archivist of magmatic crystallization conditions: Problems, potential, and implications for inferring magma storage prior to the paroxysmal 2010 eruption of Mount Merapi, Indonesia: Contributions to Mineralogy and Petrology, v. 167, article 1016, doi: 10.1007/s00410-014-1016-4.

Ghiorso, M., and Gualda, G., 2015, An H_2O-CO_2 mixed fluid saturation model compatible with rhyolite-MELTS: Contributions to Mineralogy and Petrology, v. 169, p. 1–30.

Grondahl, C., and Zajacz, Z., 2017, Magmatic controls on the genesis of porphyry Cu-Mo-Au deposits: The Bingham Canyon example: Earth and Planetary Science Letters, v. 480, p. 53–65.

Hammarstrom, J.M., and Zen, E.A., 1986, Aluminum in hornblende; an empirical igneous geobarometer: American Mineralogist, v. 71, p. 1297–1313.

Hawthorne, F.C., Oberti, R., Harlow, G.E., Maresch, W.V., Martin, R.F., Schumacher, J.C., and Welch, M.D., 2012, IMA report: Nomenclature of the amphibole supergroup: American Mineralogist, v. 97, p. 2031–2048.

Hollister, L.S., Grissom, G.C., Peters, E.K., Stowell, H.H., and Sisson, V.B., 1987, Confirmation of the empirical correlation of Al in hornblende with pressure of solidification of calc-alkaline plutons: American Mineralogist, v. 72, p. 231–239.

Holwell, D.A., Fiorentini, M., McDonald, I., Lu, Y.J., Giuliani, A., Smith, D., Keith, M., and Locmelis, M., 2019, A metasomatized lithospheric mantle control on the metallogenic signature of post-subduction magmatism: Nature Communications, doi: 10.1038/s41467-019-11065-4.

Hou, Z.Q., Ma, H., Zaw, K., Zhang, Y.Q., Wang, M.J., Wang, Z., Pan, G.T., and Tang, R.L., 2003, The Himalayan Yulong porphyry copper belt: Product of large-scale strike-slip faulting in eastern Tibet: Economic Geology, v. 98, p. 125–145.

Hou, Z.Q., Gao, Y.F., Qu, X.M., Rui, Z.Y., and Mo, X.X., 2004, Origin of adakitic intrusives generated during mid-Miocene east-west extension in southern Tibet: Earth and Planetary Science Letters, v. 220, p. 139–155.

Hou, Z.Q., Zheng, Y.C., Yang, Z.M., Rui, Z.Y., Zhao, Z.D., Jiang, S.H., Qu, X.M., and Sun, Q.Z., 2013, Contribution of mantle components within juvenile lower-crust to collisional zone porphyry Cu systems in Tibet: Mineralium Deposita, v. 48, p. 173–192.

Hou, Z.Q., Yang, Z.M., Lu, Y.J., Kemp, A., Zheng, Y.C., Li, Q.Y., Tang, J.X., Yang, Z.S., and Duan, L.F., 2015, A genetic linkage between subductionand collision-related porphyry Cu deposits in continental collision zones: Geology, v. 43, p. 247–250.

Huang, M.L., Bi, X.W., Richards, J.P., Hu, R.Z., Xu, L.L., Gao, J.F., Zhu, J.J., and Zhang, X.C., 2019a, High water contents of magmas and extensive fluid exsolution during the formation of the Yulong porphyry Cu-Mo deposit, eastern Tibet: Journal of Asian Earth Sciences, v. 176, p. 168–183.

Huang, M.L., Zhu, J.J., Bi, X.W., Xu, L.L., Xu, Y., 2022, Low magmatic Cl contents in giant porphyry Cu deposits caused by early fluid exsolution: A case study of the Yulong belt and implication for exploration: Ore Geology Reviews, v. 141, article 104664.

Humphreys, M.C.S., Smith, V.C., Coumans, J.P., Riker, J.M., Stock, M.J., de Hoos, J.C.M., and Brooker, R.A., 2021, Rapid pre-eruptive mush reorganisation and atmospheric volatile emissions from the 12.9 ka Laacher See eruption, determined using apatite: Earth and Planetary Science Letters, v. 576, article 117198.

Hutchinson, M.C., and Dilles, J.H., 2019, Evidence for magmatic anhydrite in porphyry copper intrusions: Economic Geology, v. 114, p. 143–152.

Imai, A., 2001, Generation and evolution of ore fluids for porphyry Cu-Au mineralization of the Santo Tomas II (Philex) deposit, Philippines: Resource Geology, v. 51, p. 71–96.

——2002, Metallogenesis of porphyry Cu deposits of the western Luzon arc, Philippines: K-Ar ages, S contents of microphenocrystic apatite and significance of intrusive rocks: Resource Geology, v. 52, p. 147–161.

Ishihara, S., and Imai, A., 2014, Oxidized granitic magmas and porphyry copper mineralization, *in* Kumar, S., and Singh, R.N., eds., Modelling of magmatic and allied processes: Society of Earth Scientists Series, Springer International Publishing Switzerland, p. 209–223.

Johnson, M.C., and Rutherford, M.J., 1989, Experimental calibration of the aluminum-in-hornblende geobarometer with application to Long Valley caldera (California) volcanic rocks: Geology, v. 17, p. 837–841.

Journeau, C., Shapiro, N.M., Seydoux, L., Soubestre, J., Koulakov, I.Y., Jakovlev, A.V., Abkadyrov, I., Gordeev, E.I., Chebrov, D.V., Droznin, D.V., Sens-Schonfelder, C., Luehr, B.G., Tong, F., Farge, G., and Jaupart, C., 2022, Seismic tremor reveals active trans-crustal magmatic system beneath Kamchatka volcanoes: Science Advances, v. 8, article eabj1571.

Kendall-Langley, L.A., Kemp, A.I.S., Hawkesworth, C.J., E.I.M.F., and Roberts, M.P., 2021, Quantifying F and Cl concentrations in granitic melts from apatite inclusions in zircon: Contributions to Mineralogy and Petrology, v. 176, article 58.

Ketcham, R.A., 2015, Calculation of stoichiometry from EMP data for apatite and other phases with mixing on monovalent anion sites: American Mineralogist, v. 100, p. 1620–1623.

Landtwing, M.R., Furrer, C., Redmond, P.B., Pettke, T., Guillong, M., and Heinrich, C.A., 2010, The Bingham Canyon porphyry Cu-Mo-Au deposit III. Zoned copper-gold ore deposition by magmatic vapor expansion: Economic Geology, v. 105, p. 91–118.

Large, S.J.E., Buret, Y., Wotzlaw, J.F., Karakas, O., Guillong, M., von Quadt, A., and Heinrich, C.A., 2021, Copper-mineralised porphyries sample the evolution of a large-volume silicic magma reservoir from rapid assembly to solidification: Earth and Planetary Science Letters, v. 563, article 116877.

Li, H., and Hermann, J., 2017, Chlorine and fluorine partitioning between apatite and sediment melt at 2.5 GPa, 800°C: A new experimentally derived thermodynamic model: American Mineralogist, v. 102, p. 580–594.

Li, J.X., Li, G.M., Evans, N.J., Zhao, J.X., Qin, K.Z., and Xie, J., 2021, Primary fluid exsolution in porphyry copper systems: Evidence from magmatic apatite and anhydrite inclusions in zircon: Mineralium Deposita, v. 56, p. 407–415.

Li, W.K., Yang, Z.M., Cao, K., Lu, Y.J., and Sun, M.Y., 2019, Redox-controlled generation of the giant porphyry Cu-Au deposit at Pulang, southwest China: Contributions to Mineralogy and Petrology, v. 174, article 12, doi: 10.1007/s00410-019-1546-x.

Li, W., and Costa, F., 2020, A thermodynamic model for F-Cl-OH partitioning between silicate melts and apatite including non-ideal mixing with application to con-straining melt volatile budgets: Geochimica et Cosmochimica Acta, v. 269, p. 203–222.

Li, W., Chakraborty, S., Nagashima, K., and Costa, F., 2020, Multicomponent diffusion of F, Cl and OH in apatite with application to magma ascent rates: Earth and Planetary Science Letters, v. 550, article 116545.

Li, Y., Selby, D., Condon, D., and Tapster, S., 2017, Cyclic magmatic-hydrothermal evolution in porphyry systems: High-precision U-Pb and Re-Os geochronology constraints from the Tibetan Qulong porphyry Cu-Mo deposit: Economic Geology, v. 112, p. 1419–1440.

Loucks, R.R., 2014, Distinctive composition of copper-ore-forming arc magmas: Australian Journal of Earth Science, v. 61, p. 5–16

Lu, Y.J., Kerrich, R., Kemp, A.I.S., McCuaig, T.C., Hou, Z.Q., Hart, C.J.R., Li, Z.X., Cawood, P.A., Bagas, L., Yang, Z.M., Cliff, J., Belousova, E.A., Jourdan, F., and Evans, N.J., 2013, Intracontinental Eocene-Oligocene porphyry Cu mineral systems of Yunnan, western Yangtze craton, China: Compositional characteristics, sources, and implications for continental collision metallogeny: Economic Geology, v. 108, p. 1541–1576.

Lu, Y.J., Loucks, R.R., Fiorentini, M.L., Yang, Z.M., and Hou, Z.Q., 2015, Fluid flux melting generated postcollisional high Sr/Y copper ore-forming water-rich magmas in Tibet: Geology, v. 43, p. 583–586.

Mao, M., Rukhlov, A.S., Rowins, S.M., Spence, J., and Coogan, L.A., 2016, Apatite trace element compositions: A robust new tool for mineral exploration: Economic Geology, v. 111, p. 1187–1222.

Marks, M.A.W., Scharrer, M., Ladenburger, S., and Markl, G., 2016, Comment on "Apatite: a new redox proxy for silica magmas?": Geochimica et Cosmochimica Acta, v. 183, p. 267–270.

McCubbin, F.M., Vander Kaaden, K.E., Tartèse, R., Boyce, J.W., Mikhail, S., Whitson, E.S., Bell, A.S., Anand, M., Franchi, I.A., Wang, J., and Hauri, E.H., 2015, Experimental investigation of F, Cl, and OH partitioning between apatite and Fe-rich basaltic melt at 1.0–1.2 GPa and 950–1000°C: American Mineralogist, v. 100, p. 1790–1802.

Melekhova, E., Blundy, J., Martin, R., Arculus, R., and Pichavant, M., 2017, Petrological and experimental evidence for differentiation of water-rich magmas beneath St. Kitts, Lesser Antilles: Contribution to Mineralogy and Petrology, v. 172, article 98.

Mutch, E., Blundy, J., Tattitch, B., Cooper, F., and Brooker, R., 2016, An experimental study of amphibole stability in low-pressure granitic magmas and a revised Al-in-hornblende geobarometer: Contributions to Mineralogy and Petrology, v. 171, p. 85.

Nathwani, C.L., Loader, M.A., Wilkinson, J.J., Buret, Y., Sievwright, R.H., and Hollings, P., 2020, Multi-stage arc magma evolution recorded by apatite in volcanic rocks: Geology, v. 48, p. 323–327.

Newman, S., and Lowenstern, J.B., 2002, VolatileCalc: A silicate melt-H_2O-CO_2 solution model written in Visual Basic for excel: Computers & Geosciences, v. 28, p. 597–604.

Pan, L.C., Hu, R.Z., Wang, X.S., Bi, X.W., Zhu, J.J., and Li, C., 2016, Apatite trace element and halogen compositions as petrogenetic-metallogenic indicators: Examples from four granite plutons in the Sanjiang region, SW China: Lithos, v. 254–255, p. 118–130.

Pan, Y., and Fleet, M.E., 2002, Compositions of the apatite-group minerals: Substitution mechanisms and controlling factors: Reviews in Mineralogy and Geochemistry, v. 48, p. 13–49.

Piccoli, P.M., and Candela, P.A., 2002, Apatite in igneous systems: Reviews in Mineralogy and Geochemistry, v. 48, p. 255–292.

Putirka, K., 2016, Amphibole thermometers and barometers for igneous systems and some implications for eruption mechanisms of felsic magmas at arc volcanoes: American Mineralogist, v. 101, p. 841–858.

Qin, K.Z., Xia, D.X., Li, G.M., Xiao, B., Duo, J., Jiang, G.W., and Zhao, J.X., 2014, Qulong porphyry-skarn Cu-Mo deposit, Tibet: Science Press, Beijing (In Chinese).

Richards, J.P., 2003, Tectono-magmatic precursors for porphyry Cu-(Mo-Au) deposit formation: Economic Geology, v. 98, p. 1515–1533.

——2009, Postsubduction porphyry Cu-Au and epithermal Au deposits: Products of remelting of subduction-modified lithosphere: Geology, v. 37(3), p. 247–250.

—2011, Magmatic to hydrothermal metal fluxes in convergent and collided margins: Ore Geology Reviews, v. 40, p. 1–26.

Richards, J.P., López, G.P., Zhu, J.-J., Creaser, R.A., Locock, A.J., and Mumin, A.H., 2017, Contrasting tectonic settings and sulfur contents of magmas associated with Cretaceous porphyry Cu ± Mo ± Au and intrusion-related iron oxide Cu-Au deposits in northern Chile: Economic Geology, v. 112, p. 295–318.

Ridolfi, F., and Renzulli, A., 2012, Calcic amphiboles in calc-alkaline and alkaline magmas: Thermobarometric and chemometric empirical equations valid up to 1,130°C and 2.2 GPa: Contributions to Mineralogy and Petrology, v. 163, p. 877–895.

Ridolfi, F., Renzulli, A., and Puerini, M., 2010, Stability and chemical equilibrium of amphibole in calc-alkaline magmas: An overview, new thermobarometric formulations and application to subduction-related volcanoes: Contributions to Mineralogy and Petrology, v. 160, p. 45–66.

Schmidt, M.W., 1992, Amphibole composition in tonalite as a function of pressure: An experimental calibration of the Al-in-hornblende barometer: Contributions to Mineralogy and Petrology, v. 110, p. 304–310.

Sha, L.K., and Chappell, B.W., 1999, Apatite chemical composition, determined by electron microprobe and laser-ablation inductively coupled plasma mass spectrometry, as a probe into granite petrogenesis: Geochimica et Cosmochimica Acta, v. 63, p. 3861–3881.

Shafiei, B., Haschke, M., and Shahabpour, J., 2009, Recycling of orogenic arc crust triggers porphyry Cu mineralization in Kerman Cenozoic arc rocks, southeastern Iran: Mineralium Deposita, v. 44, p. 265–283.

Shinohara, H., 1994, Exsolution of immiscible vapor and liquid phases from a crystallizing silicate melt: Implications for chlorine and metal transport: Geochimica et Cosmochimica Acta, v. 58, p. 5215–5221.

Shinohara, H., and Hedenquist, J.W., 1997, Constraints on magma degassing beneath the Far Southeast porphyry Cu-Au deposit, Philippines: Journal of Petrology, v. 38, p. 1741–1752.

Sillitoe, R.H., 1998, Major regional factors favoring large size, high hypogene grade, elevated gold content and supergene oxidation and enrichment of porphyry copper deposits, *in* Porter, T.M., ed., Porphyry and hydrothermal copper and gold deposits: A global perspective, Perth, 1998, conference proceedings: Glenside, South Australia, Australian Mineral Foundation, p. 21–34.

——2010, Porphyry copper systems: Economic Geology, v. 105, p. 3–41.

Stock, M.J., Humphreys, M.C.S., Smith, V.C., Isaia, R., Brooker, R.A., and Pyle, D.M., 2018, Tracking volatile behaviour in sub-volcanic plumbing systems using apatite and glass: Insights into pre-eruptive processes at Campi Flegrei, Italy: Journal of Petrol, v. 59, p. 2463–2491.

Streck, M.J., and Dilles, J.H., 1998, Sulfur evolution of oxidized arc magmas as recorded in apatite from a porphyry copper batholith: Geology, v. 26, p. 523–526.

Tattitch, B., Chelle-Michou, C., Blundy, J., and Loucks, R.R., 2021, Chemical feedbacks during magma degassing control chlorine partitioning and metal extraction in volcanic arcs: Nature Communications, v. 12, article 1774.

Thomas, W., and Ernst, W.G., 1990, The aluminum content of hornblende in calcalkaline granitic rocks; a mineralogic barometer calibrated experimentally to 12 kbars: Geochemical Society, Spec Publication 2, p. 59–63.

Tosdal, R.M., and Richards, J.P., 2001, Magmatic and structural controls on the development of porphyry Cu ± Mo ± Au deposits: Reviews in Economic Geology, v. 14, p. 157–181.

Wang, C.G., Yang, L.Q., and He, W.Y., 2017, Apatite trace element and halogen compositions from the Beiya gold deposit, in western Yunnan and geological significance: Acta Petrologica Sinica, v. 33, p. 2213–2224.

Wang, D., Bi, X.W., Zhou, T., Zhang, W.L., Wang, X.S., and Xu, L.L., 2013, Volatile abundances in apatite from alkaline magma in the Jinshajiang-Honghe in continental tectonic setting: Acta Mineralogica Sinica, v. 33, p. 231–238.

Webster, J.D., Baker, D.R., and Aiuppa, A., 2018, Halogens in mafic and intermediate-silica content magmas, *in* Harlow, D., and Aranovich, L.Y., eds., The role of halogens in terrestrial and extraterrestrial geochemical processes: Surface, crust, and mantle: Springer International Publishing, 1030 p.

Webster, J.D., Tappen, C.M., and Mandeville, C.W., 2009, Partitioning behavior of chlorine and fluorine in the system apatite–melt–fluid. II: Felsic silicate systems at 200 MPa: Geochimica et Cosmochimica Acta, v. 73, p. 559–581.

Xiao, B., Qin, K., Li, G., Li, J., Xia, D., Chen, L., and Zhao, J., 2012, Highly oxidized magma and fluid evolution of Miocene Qulong giant porphyry Cu-Mo deposit, southern Tibet, China: Resource Geology, v. 62, p. 4–18.

Xie, F.W., Tang, J.X., Chen, Y.C., and Lang, X.H., 2018, Apatite and zircon geochemistry of Jurassic porphyries in the Xiongcun district, southern Gangdese porphyry copper belt: Implications for petrogenesis and mineralization: Ore Geology Reviews, v. 96, p. 98–114.

Xing, K., Shu, Q.H., Lentz, D.R., and Wang, F.Y., 2020, Zircon and apatite geochemical constraints on the formation of the Huojihe porphyry Mo deposit in the Lesser Xing'an Range, NE China: American Mineralogist, v. 105, p. 382–396.

Xu, L.L., Bi, X.W., Hu, R.Z., Zhang, X.C., Su, W.C., Qu, W.J., Hu, Z.C., and Tang, Y.Y., 2012, Relationships between porphyry Cu-Mo mineralization in the Jinshajiang-Red River metallogenic belt and tectonic activity: Constraints from zircon U-Pb and molybdenite Re-Os geochronology: Ore Geology Reviews, v. 48, p. 460–473.

Xu, L.L., Bi, X.W., Hu, R.Z., Qi, Y.Q., Tang, Y.Y., Wang, X.S., and Zhu, J.J., 2016, Redox states and genesis of magmas associated with intra-continental porphyry Cu-au mineralization within the Jinshajiang-Red River alkaline igneous belt, SW China: Ore Geology Reviews, v. 73, p. 330–345.

Xu, L.L., Zhu, J.J., Huang, M.L., Pan, L.C., Hu, R.Z., and Bi, X.W., 2023, Genesis of hydrous-oxidized parental magmas for porphyry Cu (Mo, Au) deposits in a postcollisional setting: Examples from the Sanjiang region, SW China: Mineralium Deposita, v. 58, p. 161–196, doi: 10.1007/s00126-022-01143-x.

Yang, Z.M., and Cooke, D., 2019, Porphyry copper deposits in China: Society of Economic Geologists, v. 22, p. 133–187.

Yang, Z.M., Lu, Y.J., Hou, Z.Q., and Chang, Z.S., 2015, High-Mg diorite from Qulong in southern Tibet: Implications for the genesis of adakite-like

intrusions and associated porphyry Cu deposits in collisional orogens: Journal of Petrology, v. 56, p. 227–254.

Yang, Z.M., Goldfarb, R., and Chang, Z.S., 2016, Generation of postcollisional porphyry copper deposits in southern Tibet triggered by subduction of the Indian continental plate: Society of Economic Geologists, Special Publication 19, p. 279–300.

Zafar, T., Leng, C.B., Zhang, X.C., and Rehman, H.U., 2019, Geochemical attributes of magmatic apatite in the Kukaazi granite from western Kunlun orogenic belt, NW China: Implications for granite petrogenesis and Pb-Zn (-Cu-W) mineralization: Journal of Geochemical Exploration, v. 204, p. 256–269.

Zajacz, Z., Seo, J.H., Candela, P.A., Piccoli, P.M., and Tossell, J.A., 2011, The solubility of copper in high-temperature magmatic vapors: A quest for the significance of various chloride and sulfide complexes: Geochimica et Cosmochimica Acta, v. 75, p. 2811–2827.

Zentilli, M., Maksaev, V., Boric, R., and Wilson, J., 2018, Spatial coincidence and similar geochemistry of Late Triassic and Eocene-Oligocene magmatism in the Andes of northern Chile: Evidence from the MMH porphyry type Cu-Mo deposit, Chuquicamata District: International Journal of Earth Sciences, v. 107, p. 1097–1126.

Zhang, D.H., and Audétat, A., 2017, What caused the formation of the giant Bingham Canyon porphyry Cu-Mo-Au deposit? Insights from melt inclusions and magmatic sulfides: Economic Geology, v. 112, p. 221–244.

Zheng, Y.F., Mao, J.W., Chen, Y.J., Sun, W.D., Ni, P., and Yang, X.Y., 2019, Hydrothermal ore deposits in collisional orogens: Science Bulletin, v. 64, p. 205–212.

Zhong, S.H., Feng, C.Y., Seltmann, R., Li, D.X., and Dai, Z.H., 2018, Geochemical contrasts between Late Triassic ore-bearing and barren intrusions in the Weibao Cu–Pb–Zn deposit, East Kunlun Mountains, NW China: constraints from accessory minerals (zircon and apatite): Mineralium Deposita, v. 53 (6), p. 855–870.

Zhou, T.F., Wang, S.W., Fan, Y., Yuan, F., Zhang, D.Y., and White, N.C., 2015, A review of the intracontinental porphyry deposits in the Middle-Lower Yangtze River Valley metallogenic belt, Eastern China: Ore Geology Reviews, v. 65, p. 433–456.

Zhu, J.J., Richards, J.P., Rees, C., Creaser, R., DuFrane, S.A., Locock, A., Petrus, J.A., and Lang, J., 2018, Elevated magmatic sulfur and chlorine contents in ore-forming magmas at the Red Chris porphyry Cu-Au deposit, northern British Columbia, Canada: Economic Geology, v. 113, p. 1047–1075.

Zhu, J.J., Hu, R.Z., Bi, X.W., Hollings, P., Zhong, H., Gao, J.F., Pan, L.C., Huang, M.L., and Wang, D.Z., 2022, Porphyry Cu fertility of eastern Paleo-Tethyan arc magmas: Evidence from zircon and apatite compositions: Lithos, v. 424, article 106775.

Zirner, A., Marks, M.A.W., Wenzel, T., Jacob, D.E., and Markl, G., 2015, Rare earth elements in apatite as a monitor of magmatic and metasomatic processes: The Ilimaussaq complex South Greenland: Lithos, v. 228–229, p. 12–72.

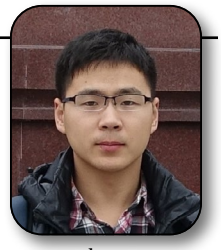

Ming-Liang Huang is currently a postdoctoral fellow at the Institute of Geochemistry, Chinese Academy of Sciences. He earned his B.Sc. degree (2014) from Jilin University and completed his Ph.D. degree (2019) at the Institute of Geochemistry, Chinese Academy of Sciences. Ming-Liang conducted cooperative research at Laurentian University as a visiting student in 2018. His research focuses on the magmatism and genesis of postsubduction porphyry Cu deposits.